From domain engineering to domain-wall engineering

Mael Guennou

Mémoire d'habilitation à diriger les recherches

Sorbonne Université

Soutenue le 29 juin 2018 à Paris

From domain engineering to domain-wall engineering

Contributions to ferroic studies

Mael Guennou

Luxembourg Institute of Science and Technology

Composition du jury

Pr. A. Gauzzi	Sorbonne Université, France		Examinateur
Pr. M. Gregg	Université Queen's de Belfast, Royaume-Uni		Examinateur
Pr. B. Hehlen	Université de Montpellier, France	Rapporteur	Examinateur
Pr. D. Lupascu	Université de Duisburg-Essen, Allemagne		Examinateur
Pr. B. Malič	Institut Jožef Stefan, Slovénie	Rapportrice	Examinatrice
Pr. S. Picozzi	CNR-SPIN, Italie	Rapportrice	
Pr. W. Schranz	Université de Vienne, Autriche		Examinateur

Contents

Foreword

This dissertation summarizes research works carried out from my PhD to the most recent years. Going back in time as far as 2007 to topics that are no longer under the spotlight may seem of limited interest, but it was found useful to underline the continuity in my research. It gives its title to this memoir: *From domain engineering to domain-wall engineering*, a title chosen because it corresponds to my experience, and also mirrors the evolution of a field and a community.

The manuscript is divided into two parts. The first part covers the core of my past work. The organization is loosely chronological, and shows a summary of my studies of phase transitions and domain engineering, up to the most recent works on ferroic domain walls. The chronology is reflected in the weights given to the different topics: older works are reduced to brief descriptions while more emphasis is laid on the most recent results, especially those obtained together with the PhD students I have co-supervised.

The second part, *From current to future works*, reports on some more recent studies that give the directions for my future research in the short term. They are being continued right now through projects that are starting or about to start.

Some results have been left aside, notably the work on nickelate thin films covered by the recent PhD work of A. Schober, as well as the fruitful work done in collaboration with the University of Luxembourg over the past 5 years.

I would like to express here ma gratitude to the many dedicated people I have been honoured to work with over the past 10 years. I think of research as a team work, and have always been happy to find in colleagues and students complementarities in skills, vision and character. I am particularly thankful to my PhD supervisor Hichem Dammak, as well as Jens Kreisel, Pierre Bouvier, Jirka Hlinka and Emmanuel Defaÿ. I also would like to thank the PhD students whose works are reported here: Mads Weber, Guillaume Nataf and Alexander Schober.

Part I
From domain engineering to domain-wall engineering

1 – Introduction

This introductory chapter deals with ferroic transitions in general. Its purpose is to lay the basic definitions and notions of ferroic transitions, domains and domain walls that will be used throughout this document, with some emphasis on symmetry-based definitions and properties. Since most of my work has been devoted to oxides with the perovskite structure, this part will also go into specific aspects of ferroic transitions in perovskites as they are usually described, with tilting of the octahedra network, ferroelectric transitions, and Jahn-Teller distortions, alone or in combination.

1.1 – Definitions

Ferroic phase transitions

There are several approaches to ferroic materials. In the context of public outreach, they are probably best explained as "materials with a memory": they can exist in several equivalent states and can be switched back and forth between these states by application of appropriate fields, typically stress, electric and magnetic fields, for the most common. They can therefore store a bit of information that can be read and written. This approach to ferroic materials corresponds to the definition initally proposed by Aizu who coined the term in the early 70's [1]. Another approach is to define a ferroic *phase transition*. I will follow here the definition adopted by V. Wadhawan [2]:

> *A phase transition is called a ferroic transition if: (a) it can be viewed as a nondisruptive modification of a certain "prototypic phase", and (b) it involves a loss of one or more point-symmetry operators present in the prototype.*

Following this definition, ferroelectric transitions correspond to a loss of inversion symmetry, (anti)ferromagnetic transitions to the loss of time-inversion symmetry, and ferroelastic transitions to the loss of symmetry elements such as mirror planes or rotation axis. Basic illustrations of a ferroelastic and a ferroelectric transition are depicted in Fig. 1.1.

Ferroic domains and domain boundaries

A ferroic transition leads to the formation of domains, i.e. regions that are equivalent by symmetry, but have different orientations in space. If G and F are the point groups of the prototypic phase and the ferroic phase respectively, then the number of these domains is simply given by the index

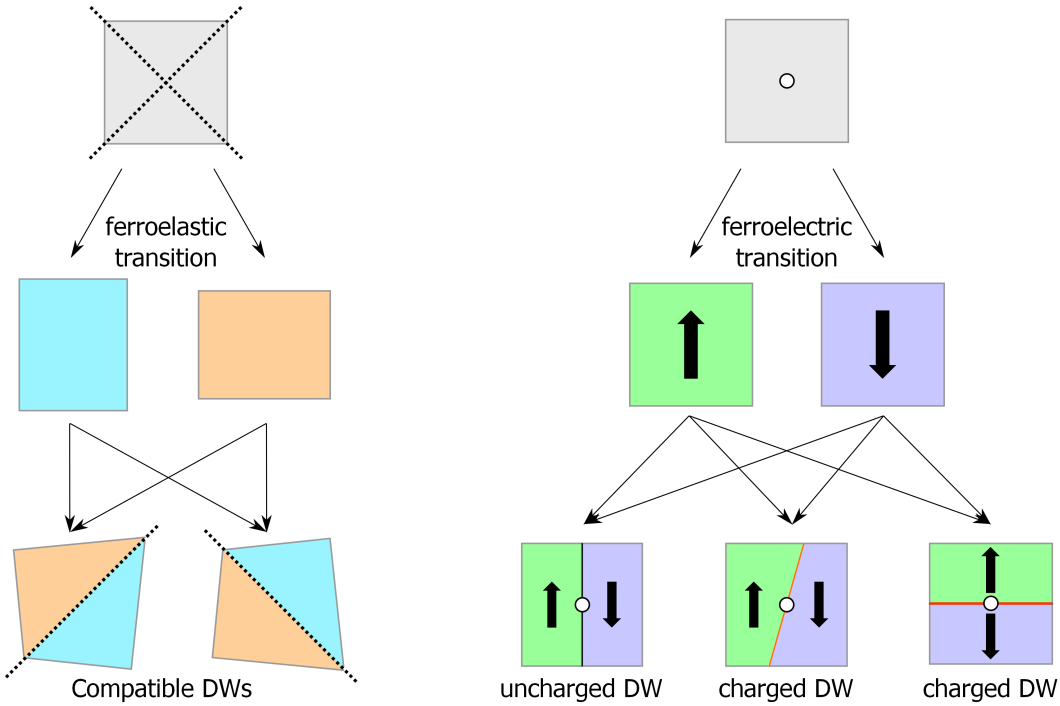

Figure 1.1: Schematic representations of elementary ferroic transitions. In the ferroelastic case (left), the two domains combine into two different domain pairs separated by compatible walls, which here coincide with the mirror planes lost at the transition. Mind the small rotation that is necessary to bring the two domains in contact with each other. In the ferroelectric case (right), examples of charged and uncharged domain walls are shown. The orientation of the walls is not fixed by symmetry or strain.

of F in G. The domains are related to one another by the symmetry operations lost at the phase transition.

Symmetry-wise, the formation of domains can be seen as an application of the Curie principle. According to this principle, the symmetry of the effect cannot be lower than the symmetry of the cause, so that a change in a scalar – and totally symmetric – parameter such as temperature or hydrostatic pressure should not allow a crystal to lower its symmetry. The formation of domains is the process by which a crystal respects this principle: the symmetry is indeed preserved on the average, when all possible domains are taken into account.

Different domains co-existing in the material are separated by *domain walls* or *domain boundaries* that act as transition regions where the order parameter changes continuously from one domain to another. The symmetry properties of the transition does not by itself say anything about the shape or orientation in space of these boundaries in general, but there are important special cases. In ferroelastic materials, where the transition is characterized by the emergence of some spontaneous strains, domain walls are formed in a way that they minimize the elastic energy of the crystal. This is realized by forming boundaries in planes where both domains are equally strained with respect to the prototypic phase, and such walls as called *compatible* (fig. 1.1). The possible orientations of compatible domain walls have been derived for all possible symmetry descents [3–5]. It is there common to distinguish two types of walls labelled W and W'. The orientation of the former is

fixed by symmetry to some crystallographic planes, while the orientation of the latter is not, but depends on the values of coefficients of the spontaneous strain tensor.

Another useful notion in ferroelectric materials is the distinction between charged and uncharged (or neutral) domain walls. If the spontaneous polarization in domains 1 and 2 are labelled $\mathbf{P}_1$ and $\mathbf{P}_2$, and the orientation of the domain wall is given by a normal vector $\mathbf{n}$, then the surface charges at the domain walls is given by $(\mathbf{P}_1 - \mathbf{P}_2) \cdot \mathbf{n}$. The domain wall is called neutral if this charge cancels out to zero, and charged otherwise (Fig. 1.1). Generally speaking, charged domain walls are energetically less favourable.

Last, it is customary to distinguish between different types of domain walls depending on their internal structure. In so-called Ising walls, the order parameter goes to zero at the domain wall but keeps a constant direction. At Bloch walls, it keeps a constant magnitude but rotates in a plane parallel to the wall; this wall may therefore exist with two different chiralities. In Néel walls, the order parameter rotates in a plane perpendicular to the wall. These last two notions were originally introduced in magnetic materials, but that are now discussed for ferroelectric domain walls as well.

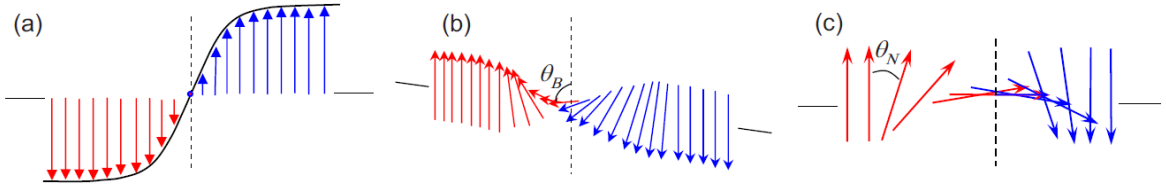

Figure 1.2: Different types of domain walls depending on their internal structure: (a) Ising, (b) Bloch, and (c) Néel. Adapted from Ref. [6].

Anti-phase domains and domain boundaries

In the case where the phase transition comes with a multiplication of the unit cell, it does not only imply the loss of point symmetry elements, but also the loss of some lattice translations. In that case, the crystal may form *antiphase domains* that are related by a lost lattice vector. Antiphase domains have the same orientation in space and identical macroscopic physical properties. They are separated by *antiphase boundaries*.

1.2 – Ferroic transition in perovskites

Most of my work is concerned with compounds with the perovskite structure. The perovskite originally designate the mineral calcium titanate $CaTiO_3$, after the russian mineralogist Lev Perovsky, and has been extended to all compounds with a similar structure: corner-sharing BO_6 octahedra defining two sites occupied by cations: the B site at the center of the octahedra and the A site between them. The interest for this structure is largely due to its extreme versatility in accepting a large number of combinations of A and B atoms, which gives rise to a wide variety of physical properties and application potentialities.

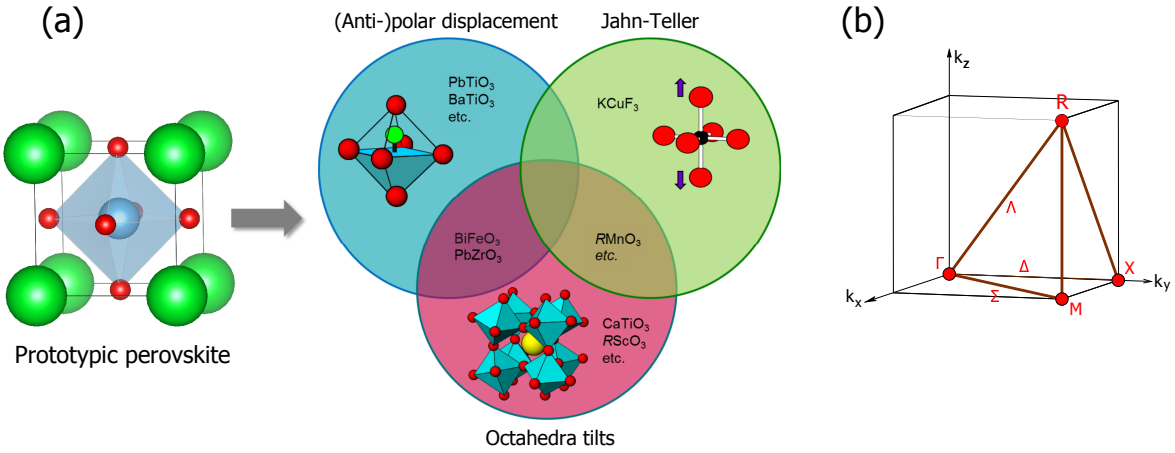

Figure 1.3: (a) Illustration of the prototypic perovskite, and the possible structural distortions. (b) Labelling of the high-symmetry points of the Brillouin zone for the simple cubic cell, as used on the Bilbao crystallographic server [7].

The high-symmetry prototypic phase of the perovskite is cubic with space group $Pm\bar{3}m$, but most compounds exhibit lower symmetries. It is useful to think of these distortions as combinations of elementary distortions illustrated in figure 1.3: octahedra tilts, (anti)polar cation displacements, and octahedra distortions. There is no one-to-one mapping between the distortions and physical properties, but they provide nonetheless useful guidelines when thinking in terms of structure and material design.

A more thorough and more rigorous description of the distortions in perovskites can be made using tools from group theory and the irreducible representations (irreps) of the prototypic space group $Pm\bar{3}m$. Their use has been greatly facilitated over the past few years by the development of programs that give the symmetry of distorted structures under combinations of several distortions [8–11], decompose distortions of a given crystal structure in symmetry adapted modes [12,13], or directly use these symmetry-adapted decompositions in structural refinements [14].

Ferroelectric transitions and cation displacements

Long-range ordered cations displacements away from their high-symmetry position is directly linked for ferroelectric properties in perovskites. Symmetry-wise, they simply correspond to a symmetry lowering from a non-polar to a polar point group, and correspond to an instability at the Γ point of the Brillouin zone. The most classical ferroelectric perovskites ($BaTiO_3$, $KNbO_3$, $PbTiO_3$) are *proper* ferroelectrics, i.e. the polarization is the primary order for the phase transition. In the search for new multiferroic materials, a lot of attention has been devoted to *improper* ferroelectricity, where the off-center cation displacement is induced by some other mechanism such as magnetism ($TbMnO_3$, $GdFeO_3$) or a combination of tilts and cation ordering.

When cations are displaced in an anti-polar arrangement, inversion symmetry is not broken. This is the principle behind antipolar or antiferroelectric materials. However, there is no example of a perovskite oxide that exhibits only antipolar cation displacements. Instead it always comes in combination with octahedra tilts.

Tilted structures

Collective rotations of octahedra, or "tilts", typically occur when the A cation is too small to fill the cuboctahedron defined by the oxygens. The cubic structure is then unstable and the octahedra network collapses on itself to reduce its volume. The symmetry aspects of tilting in perovskites were pioneered by M. Glazer [15, 16], who defined the convenient notation named after him. That was later refined and reinvestigated in order to derive systematically all possible combinations of tilts, alone or in combination with other distortions (e.g. Refs. [17–20] and references within). Those works typically consider tilt systems corresponding to instabilities at the R and M points of the Brillouin zone (Fig. 1.3), and therefore cause at most to a doubling of the perovskite unit cell along the three cubic axis leading to a $2a \times 2a \times 2a$ unit cell. This covers most of classical perovskites, but some do exhibit more complex tilt patterns ($PbZrO_3$, $NaNbO_3$, WO_3 etc.).

A very common and very important case of tilted structure is the orthorhombic *Pnma* structure. It combines two rotations of the octahedra along the [101] and [010] pseudo-cubic directions, antiphase and in-phase respectively, which is written $a^-b^+a^-$ in Glazer's notation. This structure is found in fact in a majority of perovskites [21], and is usually stable in a wide range of pressures and temperatures, to the point that phase transitions occur only at very high temperatures – if the crystal does not melt first. $CaTiO_3$ itself is such an example, with phase transitions above 1300 K.

Octahedra distortions – Jahn-Teller effect

In perovskites, the Jahn-Teller effect occurs when a transition metal cation with a partially filled $3d$ orbital occupies the B site. The Jahn-Teller effect consists in an additional distortion of the BO_6 octahedron that lifts the degeneracy of the e_g and t_{2g} energy levels of the B-cation, and thereby brings a gain in electronic energy that is larger than the elastic energy paid for the distortions of the octahedron and the lattice. Those local distortions may order on a long range and the Jahn-Teller distortion is then called cooperative. In the *Pnma* case, when present, the cooperative Jahn-Teller distortion typically has the symmetry of the irrep M_2^+ and acts as a secondary, non-symmetry-breaking order parameter [9, 10]. The most studied orthorhombic perovskites with active Jahn-Teller cations belong to the rare-earth orthomanganite family $RMnO_3$, where Mn^{3+} has a $t_{2g}^3 e_g^1$ configuration. One case where the cooperative Jahn-Teller distortion exists alone is in the fluorite $KMnF_3$.

1.3 – Two results on the Raman spectrum of perovskites

Experimentally, a large part of my work relies on structural studies of perovskites by Raman spectroscopy, i.e. measurement of phonon frequencies. In spite of the considerable amount of literature of the subject, some progress are regularly made on the general understanding on the Raman spectra of distorted perovskites; I show briefly below two recent results along that line.

The first result relates to the Raman spectrum of the rare-earth orthoferrites $RFeO_3$. They are examples of *Pnma* perovskites described above. Among their 24 Raman-active modes, two totally symmetric A_g modes are of special interest, because their atomic displacement patterns correspond directly to the two tilts of the octahedra. Those two so-called "tilt modes" have been identified in

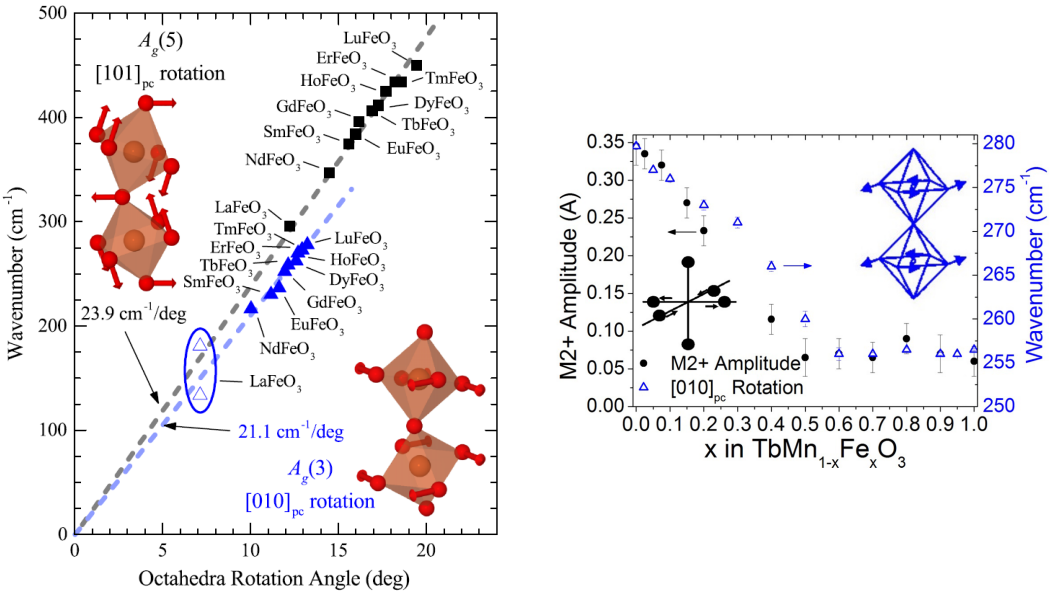

Figure 1.4: Two recent work on the Raman spectra of perovskites. Left: tilt mode frequency as a function of the tilt angle for rare-earth orthoferrites [22]. Right: Correlation between the Jahn-Teller mode and the frequency of the tilt mode [23].

a large number of compounds [22, 24, 25], and it was found that their frequencies scale linearly with the corresponding tilt angles itself. This makes Raman spectroscopy an indirect but very sensitive method to track tilt angles. We have contributed to this by verifying this linear relation in the rare-earth orthoferrites RFeO$_3$ (figure 1.4). We discussed its validity limit for large A cations, and have given physical foundations for this empirical observation with the help a simple Landau model [22].

The second result relates to the influence of Jahn-Teller distortion on the Raman spectrum of perovskites. Investigations of Jahn-Teller distortion as such are experimentally more challenging by Raman spectroscopy for several reasons. First, it comes in combination with tilts in classical perovskites and never alone in oxides. Besides, because it is not symmetry breaking, Raman spectroscopy does not allow to isolate easily its effect on the phonon modes as it can be done with the tilts. One way to isolate this contribution is to tune the Jahn-Teller effect in a continuous way. This can be done – at least at the average scale – by making a solid solution where a Jahn-Teller active cation is substituted with a non-Jahn-Teller active cation. We used this principle in a study of the Tb(Mn,Fe)O$_3$ system [23]. Figure 1.4 shows the amplitude of the Jahn-Teller distortion, as measured by the amplitude of its symmetry adapted mode, together with the Raman frequency of the [010] tilt mode. Both show correlated and non linear evolutions, which we interpret as the influence of the Jahn-Teller distortion on the tilt mode frequency. In other words, the tilt mode fequency contains contributions from for the tilts and the Jahn-Teller order parameters, the latter remaining nonetheless relatively minor (20 cm^{-1}, i.e. $\approx$10% of the Raman frequency).

2 – Domain engineering in piezoelectric single crystals

The purpose of this chapter is to account for my contributions to the studies of domain engineering in piezoelectric single crystals. This work was essentially undertaken during my PhD, with some follow-ups later on. It is an important element, in the sense that it has strongly fueled my interest for the studies of domains and domain walls that will follow in the next chapter. Yet, it is now an older piece of work, and the topic itself does no longer count among my research interests. For that reason, this chapter will be limited to a brief presentation of the context and the approach, with some results for illustration, without any attempt to provide an updated overview on the field.

2.1 – Context: giant piezoelectricity in lead-based single crystals

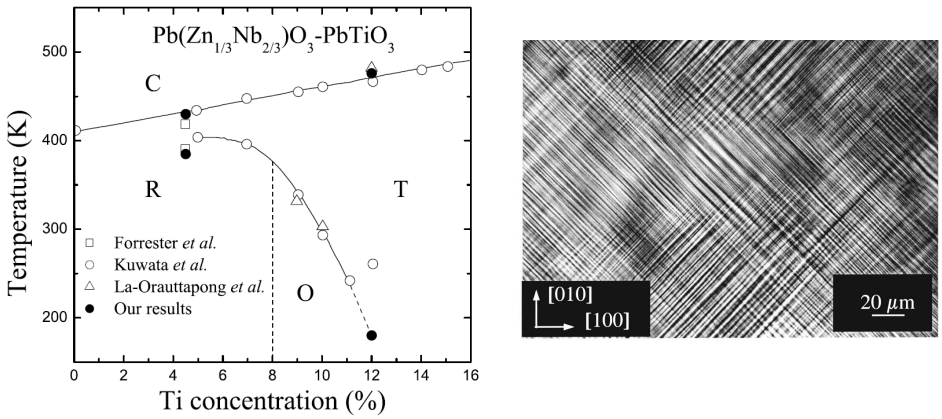

Figure 2.1: Left: x–T phase diagram of PZN-xPT from [26]. Right: Typical domain structure, seen here in a rhombohedral PMN-PT singe crystal poled along $[001]_c$.

The highest measured piezoelectric coefficients d_{33} to date have been obtained in lead-based single crystals. From their chemical composition, they are solid solutions between a relaxor ferroelectric ($PbZn_{1/3}Nb_{2/3}O_3$, $PbMg_{1/3}Nb_{2/3}O_3$, $PbSc_{1/2}Nb_{1/2}O_3$ etc.) and a classical ferroelectric ($PbTiO_3$). From a structural point of view, their composition-temperature diagram exhibits a region called *morphotropic phase boundary* (MPB) where the piezoelectric properties are maxi-

mal. Figure 2.1 shows the example of the phase diagram of $Pb(Zn_{1/3}Nb_{2/3})O_3$-$PbTiO_3$ (for short PZN-xPT) with its MPB located around $x \approx 9$ %.

The highest d_{33} are obtained when the crystals at the morphotropic compositions are poled along non-polar direction, so that the electric field stabilizes a coexistence of several ferroelectric domains, with a macroscopic symmetry that is different from the symmetry of the crystal structure. This is illustrated in Fig. 2.1 with the example of a rhombohedral crystal poled along [001] showing four variants of ferroelectric domains in a laminar arrangement. In this context, *domain engineering* can be understood as the ensemble of techniques designed to create stable domain structures in order to optimize the electromechanical properties of a material.

In multidomain crystals, one usually distinguishes *intrinsic* and *extrinsic* contributions to the macroscopic properties, the former coming from the chemical composition and orientation alone, while the latter encompasses everything else, and in particular contributions due to domain wall motion. Optimizing the electromechanical properties requires a good understanding of these different contributions. To that end, homogeneization models have been developed that relate configuration parameters (chemical composition, orientation, geometry etc.) to the final macroscopic properties.

2.2 – Approach to the homogeneization problem in PZN-PT

My work has concentrated on models of laminar domain structures, which are relevant for single crystals and correspond to the situation typically observed experimentally under a microscope. Mathematically, the effective properties of laminar piezoelectric materials is in fact easily formulated and solved (see Ref. [27] and references within). The problem was therefore not so much about solving the mathematical problem than checking its validity and its relevance. This became the core of my approach. Indeed, many assumptions in these models are sound, but have to be checked, which was far from systematic in the literature. Besides, the matrix formalism [27] is convenient, but does not allow to easily track back potential disagreements and identify their origin. We therefore derived as much as possible analytical expressions in order to track down uncertainties, identifiy dependencies, and make robust conclusions on the applicability of the model.

Choice of composition

Another – usually implicit – hypothesis is that, in the multidomain state, the intrinsic properties at the local scale within a domain can be derived from the properties measured on the single domain state by a simple change of axis. This also is not trivial: relaxor-based piezoelectric single crystals are known to exhibit complex energy landscapes in the vicinity of the MPB, and it has been shown in many cases that poling may stabilize different phases depending on the field direction, which of course yields different properties. To avoid that risk, we chose a composition $x = 12\%$ that still shows some enhancement of the piezoelectric properties, but is slightly off the MPB, so that it remains in the same tetragonal phase for all directions of the poling fields.

Determination of the intrinsic properties

Knowledge of the intrinsic properties of the materials, i.e. the properties measured on a single domain state, is essential, and usually not trivial. In the most simple case, the full electromechanical

tensor contains 11 independent coefficients (dielectric, elastic and piezoelectric constants), some of which are difficult to measure directly. A large part of the work was therefore devoted to measure those coefficients by different methods and estimate uncertainties.

We then proceeded to measure the electromechanical tensor of PZN-12%PT in its tetragonal single domain state. The main method used was the resonance-antiresonance method. The principle is to cut samples with suitable aspect ratio so as to isolate a desired vibration mode, and measure the complex impendance in its vicinity. From the position of the observed peaks, one can derive electromechanical coupling factors, as well as elastic and piezoelectric constants. Dielectric constants are measured independently at low frequencies (1–10 kHz). By using a sufficient number of samples (resp. vibration modes), the full tensor can be obtained.

The main issue with this method is that some coefficients are obtained indirectly and come with large uncertainties. This is especially dramatic for materials with high coupling factors. When applied to PZN-12%PT, we have shown that at the end of the day, some coefficients are pretty much meaningless, with uncertainties that may exceed 100% from only minor measurement errors. For that reason, this measurement was completed by two different methods: Brillouin spectroscopy (coll. P. Djémia, LPMTM, Université Paris 13), and resonance ultrasound spectroscopy (T. Delaunay, Université de Tours). The comparison between these three methods was presented in Ref. [28].

Checking the homogeneization model

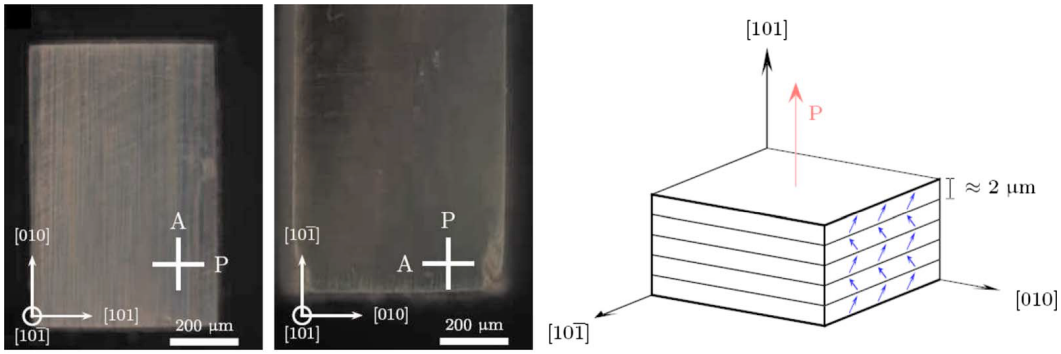

Figure 2.2: PZN-12%PT crystal poled along [110] used as a test case for the homogeneization model. Left: optical observations of the laminar domain structure. Right: sketch of the 2T domain structure. Reproduced fron Ref. [29]

The homogeneization model was then checked on PZN-12%PT poled along [110], i.e. in a laminar two-domain state, labelled 2T for 2 tetragonal domains, with macroscopic symmetry *mm*2. It was checked that this configuration produces small domains, much smaller than the crystal size, with essentially uncharged domain walls arranged in a laminar structure (Fig. 2.2). The comparison of its measured and calculated properties was presented in Ref. [29], and some of them are recalled in Table 2.1. The intrinsic value reported in the table is simply obtained by a rotation by 45° of the electromechanical tensor of the single domain.

The effective values of the piezoelectric coefficients were found to be the most insightful. As shown in Table 2.1, the agreement between the model and the experiment is very poor for d_{31}

and d_{33}, but it is good for d_{32}. When checking the expression for these effective coefficients, one realizes that d_{32} is the most simple and depends only on the intrinsic d^0_{32}, while the others involve all three piezoelectric coefficients.

We came to realize that this was due to an error in the determination of d_{15} rather than an inadequacy of the model. The shear piezoelectric coefficient is particulary delicate to measure by the resonance method because of the very high aspect ratio needed to isolate the shear vibration mode [30]. It had been strongly underestimated in our measurements, which affected greatly the values of the effective d_{31}, d_{33} and ε_{22}. In summary, the reasoning should be inverted here: measuring the piezoelectric coefficients d_{31} and d_{33} of a 2T multidomain state is a safer way to obtain indirectly the intrinsic d^0_{15} with good accuracy!

	Intrinsic value	Measured value	Calculated value	Expression
Piezoelectric coefficients [pm/V]				
d_{31}	-113	-431	-113	$(d^0_{31} + d^0_{33} - d^0_{15})/\sqrt{8}$
d_{32}	-146	-136	-146	$-d^0_{32}/\sqrt{2}$
d_{33}	349	570	349	$(d^0_{31} + d^0_{33} + d^0_{15})/\sqrt{8}$
Dielectric constants at low frequencies [ε_0]				
ε_{11}	5375	975	846	N/A
ε_{22}	10000	6300	8690	$\varepsilon^0_{22} - (d^0_{24})^2/(s^0_{44} + s^0_{66})$
ε_{33}	5375	6000	5375	$(\varepsilon^0_{11} + \varepsilon^0_{33})/2$

Table 2.1: Validation of the homogeneization model for a PZN-12%PT crystal poled along [110]. The coefficients a^0_{ij} in the expressions stand for the properties of the single tetragonal domain state in its crystallographic axes. Expressions for ε_{11} are more complex and are not commented on here.

Another interesting observation from table 2.1 is that all calculated piezoelectric coefficients are identical to their intrinsic value. In other words, the coexistence of several domains plays no role in that case for the main piezoelectric coefficients. It does affects the transverse dielectric constants ε_{11} and ε_{22}, because of the coundary conditions that the walls impose on the domains. This is also valid for rhombohedral crystals poled along [001] an their record piezoelectric coefficients: the very high d_{33} is essentially a direct consequence of the very high d_{15}, and have little to do with the geometrical arrangements of domains.

In piezoelectric single crystals, this peculiarity that the d_{33} is larger when measured at an angle from the polar axis depends on the relative strength on the piezoelectric coefficients. It occurs when the intrinsic d_{15} of the single domain exceeds some critical value, which quantifies the ability of polarization to "rotate" under the application of a transverse electric field. Following the classification by Davis *et al.* [31], materials with this property can be called "rotator" piezoelectrics while the others can be called "extender" piezoelectrics, and have the strongest response along their polar axis. In the latter, no enhancement of the piezoelectric coefficient is likely to be obtained in domain-engineered crystals like the 2T configuration. This was found to be the case, for example, in the lead-free piezoelectric Mn-doped $(Na_{1/2}Bi_{1/2})TiO_3$-6%$BaTiO_3$ which I studied later in the same spirit [32].

2.3 – Beyond the homogeneization model

One of the remarkable results in domain enginering of piezoelectric crystals was the observation by S. Wada and co-workers that a decrease of the domain size enhances the piezoelectric coefficient in $BaTiO_3$ and $KNbO_3$ single crystals [33–37]. This kind of effect cannot, by construction, be captured by the homogeneization model, which assumes homogeneous fields inside domains, and are independent on the domain size. Other methods are then necessary to account for it.

In 2012, I collaborated with J. Hlinka and P. Ondrejkovic on simulation studies of piezoelectric properties of laminar domain structures in $BaTiO_3$ with charged domain walls [38]. The configuration studied is shown in figure 2.3. By phase field simulations in the framework of the Ginzburg-Landau-Devonshire model of $BaTiO_3$, this study demonstrated an enhancement of the piezoelectric coefficient with decreasing domain size, in a way that is strongly dependent on the charge compensation at the domain wall. These size effects become significant for domain sizes below 100 nm, i.e. much smaller than the domain size seen in PZN-12%PT. It was also verified that the homogeneization model gives an asymptotic value, valid in the limit of large domains and ideal charge compensation (figure 2.3).

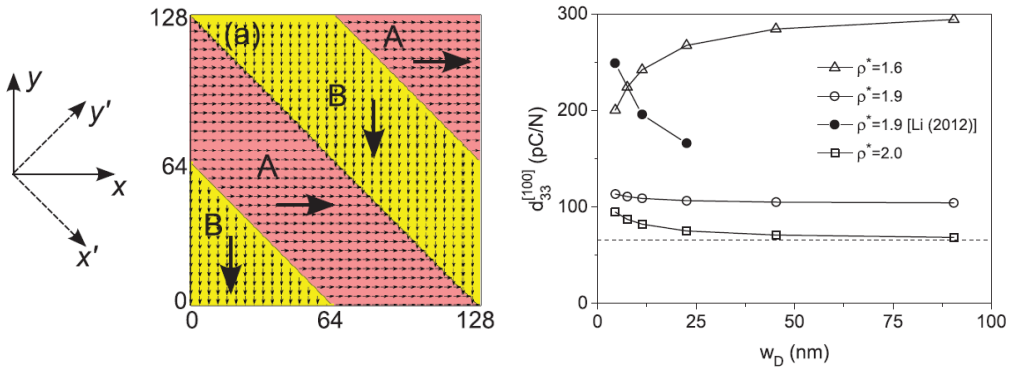

Figure 2.3: Left: domain structure considered in [38]. Right: piezoelectric coefficient as a function of domain size for several charge compensations. The dotted lines gives the effective values calculated explicitely by the laminar homogeneization model.

3 – Ferroic transitions under high pressure

The purpose of this chapter is to summarize my work on ferroic transitions under high pressure in simple perovskites. I also seize this opporunity to put forward miscellaneous observations of domain formations in high pressure phase transition, which was only back then mentioned as a side topic.

3.1 – Context: hydrostatic pressure in ferroic studies

The use of hydrostatic pressure as an external parameter to study phase transitions and corresponding changes in materials properties is admittedly less common than temperature, and certainly more recent. This has largely to do with the technical challenge of applying a hydrostatic pressure large enough to cause any significant change, while still allowing for physical measurements to be performed. Nowadays, high-pressure cells can be found as commercial setups and can be made compatible with most classical physical measurements.

The pressure range considered here goes from ambient conditions up to approximately 60 GPa (6.10^5 atm), i.e. a pressure that starts comparing to the bulk modulus of typical perovskite oxides (typically 100-300 GPa). This reduces the sample volume – and chemical bond lengths – by about 20 %, a variation that is one order of magnitude more than what is obtained with thermal expansion only. This makes the use of pressure particularly useful in perovskite studies to reveal polymorphism, stabilize new phases, and thereby shed light on the relative strengths of atomic interactions. Comparison with ab-initio DFT calculations, which have in the mean time achieved an excellent predictive power, is also much more straightforward and gives a deeper understanding of the physical mechanisms.

In perovskites, because of the links explained earlier between structural phase transitions and functional properties, our efforts have been devoted mostly to the exploration of pressure-temperature phase diagrams, with the objective to formulate general rules for the evolution of crystal structures under pressure, and the interplay between different instabilites. To that end, the emphasis was laid on textbook examples, chemically simple perovskites. Those works will be summarized in the following for each of the structural instabilities considered in the previous chapter.

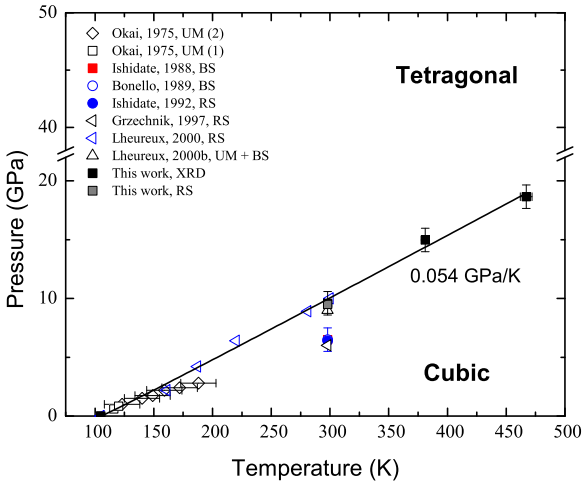

Figure 3.1: P–T phase diagrams of $SrTiO_3$ proposed in [39]

For a long time, it was believed that tilt angles in perovskites tend to always increase under pressure. From a purely geometrical point of view, this can seem intuitive, because tilting allows the crystal to reduce its volume and thereby accommodate pressure. Following the counterexample found in $LaAlO_3$, which goes from a tilted $R\bar{3}c$ to the prototypic $Pm\bar{3}m$ phase under pressure [40], these views have been revised to take into account the different compressibilities of the polyhedra in the crystal structure [41]. As a rule of thumb, one can say that $A^{3+}B^{3+}O_3$ (such as $LaAlO_3$) tend to have their tilt angle reduced under pressure, while $A^{2+}B^{4+}O_3$ (such as $SrTiO_3$) show the opposite trend. But exceptions are known, and there are multiple factors contributing, as was shown recently in a theoretical study done in collaboration with H. J. Xiang and L. Bellaiche (Univ. Arkansas, USA) [42]. Notably, in *Pnma* perovskites, it was shown that the two constitutive tilt angles may show opposite behaviours.

Experimentally, our experimental work has covered various model perovskites with tilts ($SrTiO_3$, $KMnF_3$, $CaTiO_3$, $LaAlO_3$). In all cases, the results were found consistent with the general rules. In $LaAlO_3$, we have significantly extended the pressure range investigated, and confirmed that no further phase transition was to be found up to 63 GPa [43]. In $CaTiO_3$, where the tilt angles hardly change at all up to 60 GPa, we have discussed the Raman signatures and the tilt modes in terms of compression mechanisms [44]. The most comprehensive work was done on $SrTiO_3$ [39, 45]. Its phase transition at 10 GPa from cubic to tetragonal (and tilted) $I4/mcm$ was known, but there were some open questions notably on the possibility of other phase transitions at higher pressure. In our work we have excluded any other phase transition up to 53 GPa at ambient temperature, completed the phase diagram with data points at higher temperatures, and refined the phenomenological model for the phase transition. As a textbook example of ferroelastic transition under pressure, this data has notably been used by A. Tröster and co-workers to validate a Landau model including finite strain effects [46–48]. Similar work, though less detailed, were also carried out on the isostructural fluorite $KMnF_3$ [49].

3.3 – Ferroelectricity under pressure

That classical ferroelectric perovskites ($BaTiO_3$, $PbTiO_3$ and $KNbO_3$) first undergo under pressure a transition to a paraelectric phase has been known for some time [50–53]. The proposition by DFT calculations that a ferroelectric instability might show up again in a much higher pressure range [54, 55] has motivated further experimental studies. And indeed, it was thereafter claimed, based on powder high-pressure XRD and Raman spectroscopy, that the model ferroelectric $PbTiO_3$ does undergo under pressure a phase sequence $P4mm \rightarrow Pm\bar{3}m \rightarrow I4/mcm \rightarrow I4cm$, validating these theoretical views [56]. A couple of similar claims have followed, based on Raman spectroscopy of the solid solutions (Ca,Sr)TiO_3 [57]. We clearly had this possibility in mind when investigating titanate single crystals under high pressure, but could not confirm the emergence of polar phases in $SrTiO_3$ [39] (up to 53 GPa), $CaTiO_3$ [44] (up to 60 Gpa) or single crystal $PbTiO_3$ (up to 70 GPa, unpublished work).

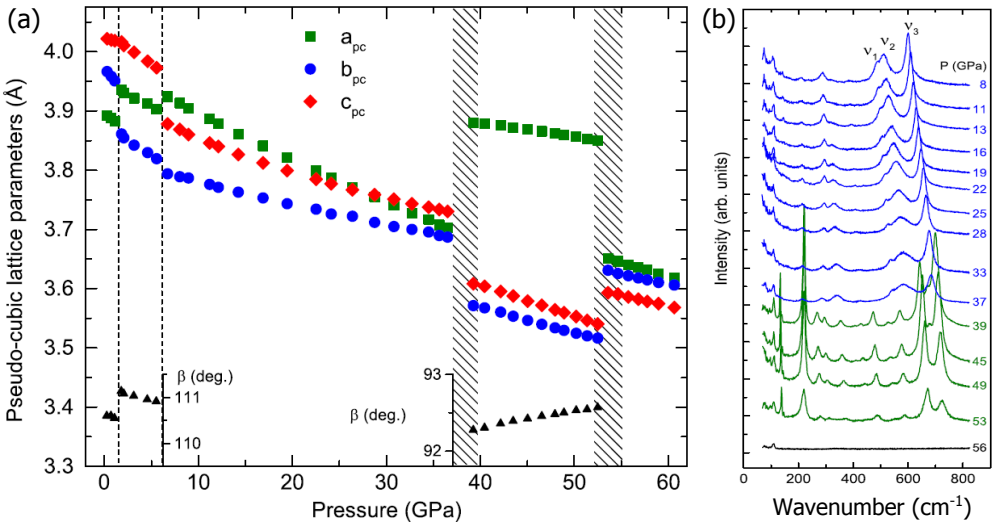

Figure 3.2: Evolution of the pseudo-cubic lattice constants of $BiMnO_3$ as a function of pressure. The very high elongation of the unit cell stable between 39 and 52 GPa is beleived to be associated to a "supertetragonal" polar phase. Reproduced from [58].

This, however, is only part of the story. The high-pressure ferroelectricity predicted in $PbTiO_3$ is displacive, soft-mode driven, and is supposed to lead to small distortions. There exists another type of polar phases in perovskites refered to as "supertetragonal" phases. They can be found in various Bi-based perovskites (as we briefly reviewed in Ref. [59]), or $PbVO_3$, and exhibit an elongation of the perovskite unit cell (c/a or equivalent) of the order of 1.2, much larger than classical ferroelectric perovskites (e.g. 1.05 for $PbTiO_3$, less for the others). In our high-pressure study of $BiMnO_3$ [58], we have identified a high pressure phase that seems to fit into that category. Figure 3.2 shows the lattice constants and the Raman spectra of $BiMnO_3$ under pressure. The combined analysis of both experiments pointed to polar space group (Cm, or $C2$), but the main argument for the polar character of this phase is the very high elongation of the unit cell, which is not found to that level in any non-polar perovskite. For comparison, we have also conducted the same study on $BiCrO_3$ single crystals (to be published), which does not show anything similar. Instead, its $Pnma$ phase remains stable on an very wide pressure range (1–70 GPa).

Following this experiment, discussions with theorists (J. Íñiguez at LIST in Luxembourg, L. Bellaiche at the Univ. Arkansas) were conducted to understand the structural results. In spite of their best efforts, and in spite of the efficiency of ab-initio methods, the experimental results could not be confirmed. Many possible phases were identified, including many that do not have a perovskite structures and could only be obtained through disruptive phase transitions, possibly triggered at high temperatures. But none of them possess the very high spontaneous strain observed experimentally in XRD. And yet the strain is an extremely robust experimental result that was observed both in powders and single crystals, and is directly visible on the diffraction pattern. To date, the structure of this phase remains an open question, and the emergence of this polar phase is in my opinion the most puzzling observation of my high-pressure studies.

3.4 – Jahn-Teller distortion under pressure

It is expected, and experimentally observed, that Jahn-Teller disortion is reduced under pressure. This has been checked in the model perovskite $KCuF_3$ [60], which exhibits only Jahn-Teller, and $LaMnO_3$ [61], where it is combined with *Pnma* tilts. The debate here relates to whether or not it can be considered completely suppressed at a high enough pressure. This question is particularly relevant for the understanding of the insulator-to-metal transition (MIT) in rare-earth manganites that occurs between 32 and 52 GPa, depending on the rare-earth [62].

The experimental difficulties associated to the study of Jahn-Teller by Raman spectroscopy have already been mentioned in chapter1. In XRD, ideally, it must be based on full Rietveld refinements, which we have in general not been able to perform with enough accuracy and reliability. As a poor man's approach, in our studies of $BiMnO_3$ [58] and $RMnO_3$ [62, 63], we analyzed the evolution of Jahn-Teller via their coupling with the spontaneous shear strain (figure 3.3), following the approach developed in Ref. [9, 10]. Long story short: this analysis does not give evidence for a suppression of the distortion at the MIT transition in the manganites for *A* cations smaller than Pr, but the evidence remains fragile and this would require further confirmation.

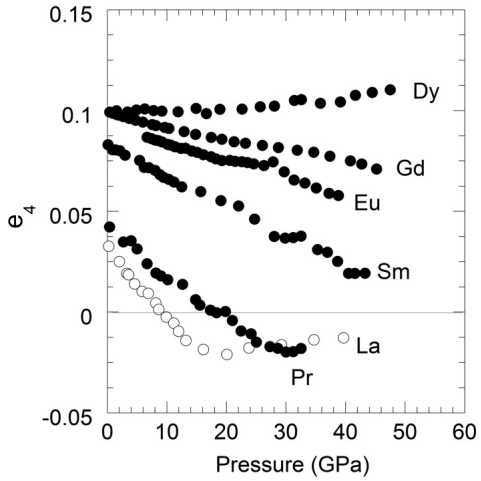

Figure 3.3: Pressure dependence of the spontaneous shear strain e_4 for different rare-earth manganites $RMnO_3$. Reproduced from Ref. [62]

3.5 – Combined instabilities: $BiFeO_3$

Bismuth ferrite $BiFeO_3$ is known as one of the very few perovskites combining at ambient conditions a strong ferroelectric polarization and magnetic order. From a pure cristallographic point of view, is also remarkable in that it combines ferroelectric displacements with tilts of octahedra ($a^-a^-a^-$ in Glazer's notation). This is in sharp contrast with $PbTiO_3$, where both instability compete: ferroelectricity has to be suppressed (at 12 Gpa) before the tilted $I4/mcm$ phase can emerge (at 20 GPa) [56]. This suggests a much richer polymorphism, which was nicely demonstrated theoretically in Ref. [64].

Our investigation of the high pressure transitions confirms this polymorphism, and we proposed an updated P–T phase diagram shown in Fig. 3.4. Between the room condition $R3c$ structure and the very stable $Pnma$ reached at 10 GPa, we found a sequence of three phase transitions [65]. In addition, we shown that the transition sequence strongly depends on the pressure transmitting medium used, i.e. the hydrostaticity of the medium [66]. The exact crystal structure of those phases is still disputable, and other papers have reported different structures [67, 68], but the following points may be agreed on. First, the unit cells are much larger than conventional perovskites, with presumably complex tilt systems that do beyond Glazer's descriptions. This has been calculated and rationalized as "nano-twins" [69]. Second, there is strong suspicion that those phases may be antiferroelectric. In the absence of dielectric measurements, this cannot be stated conclusively, but strong hints come from: i) the proposition made in Ref. [68] that the intermediate phase is isostructural with antiferroelectric $PbZrO_3$, and ii) the very strong birefringence that persists until the $Pnma$ phase (unpublished results).

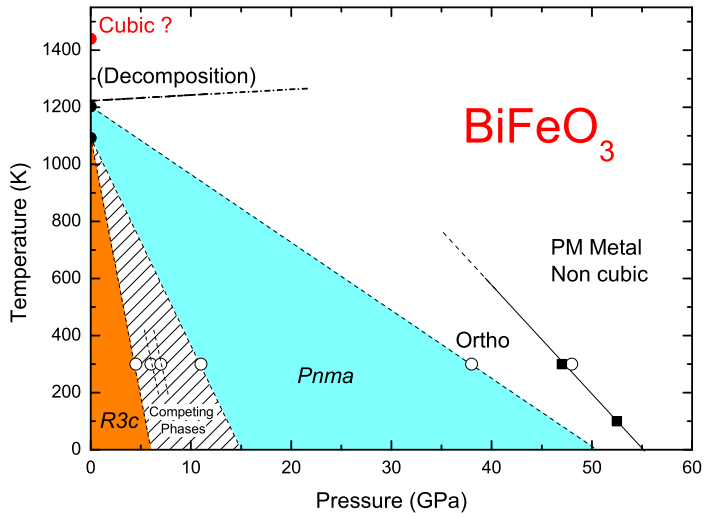

Figure 3.4: P–T phase diagrams of $BiFeO_3$ proposed in Ref. [65]

In the high pressure regime, above 30 GPa, $BiFeO_3$ was found to undergo two other phase transitions. The second one, at 48 GPa, corresponds to the insulator-to-metal transitions studied by other authors [70–72]. The two high-pressure phases have larger unit cells and increasing spontaneous strains. This again looks like an exception to the rules governing the tilts under pressure for $A^{3+}B^{3+}O_3$ perovskites. One might hypothesize that the special chemistry of bismuth and

its electron lone pair play a role here [73]. In any case, the structure does not tend to become cubic, neither does it seem to match the structure of the metallic phase identified at high temperatures [74]; the phase diagram of $BiFeO_3$ clearly requires more investigations in different P–T ranges.

3.6 – On domain formation in high-pressure phase transitions

For the crystallographer interested in the details of a crystal structure, the formation of several domains at a phase transition is usually a plague. In the context of high-pressure x-ray crystallography, where experiments are already made challenging by the diamond-anvil cell that shadows a large part of reciprocal space, absorption by the diamonds, Compton scattering, the low sensitivity of x-ray to oxygens and other technical difficulties, twinning under pressure is often the *coup de grâce* that makes any refinement impossible, and even complicates significantly the most basic analysis, typically leading to an overestimation of the symmetry.

On the other hand, poor consolation, the domain formation and evolution may also give some information. Below are explained two such cases found in the course of my high pressure studies.

Domain evolution and deviatoric stress

In a high-pressure experiment, the formation and evolution of domains can be expected to be sensitive to the hydrostaticity of the pressure conditions. In a diamond anvil cell, the stress field is described as a superposition of a hydrostatic pressure and a deviatoric stress that has the symmetry of a compressive stress along the cell axis. This symmetry breaking in turn lifts the degeneracy of the domain states, and may modify the domain structures. The symmetry treatment of that problem has been examined [75] and it is in principle possible to derive the domain structure – which may be single domain – likely to be stabilized under deviatoric stress. This is in principle found as the intersection of the point group of the stress (which would be ∞/mmm) with the point groups of the domains. In the case where the sample is randomly oriented in the cell, this will usually lift all degeneracies and lead to a single domain state.

This principle will be illustrated in experiments on $BiFeO_3$. The crystals are $[100]_{pc}$-oriented. They were always chosen as single domain states during the preparation of the experiments, but would split into many domains at the successive phase transitions, in a way that was found to depend very much on the hydrostatic conditions. Figure 3.5 summarizes the diffraction patterns for two different experiments.

In the first case, silicon oil is used as a pressure transmitting medium, which is known to provide very strong deviatoric stress [76]. Four integrated diffraction patterns are shown, illustrating the phases encountered in the low-pressure range, up to 12 GPa. The intermediate phases show very clear traces of splitting, with superstructures corresponding to the complex tilt patterns mentioned earlier. On the other hand, when the orthorhombic phase is finally reached at 12 GPa, the pattern does no longer show any sign of splitting.

The second experiment was carried out with helium as pressure-transmitting medium, which provides much better hydrostaticity. Without dwelling on the low-pressure phase transitions, figure 3.5 shows the integrated pattern obtained at 12.1 GPa. As opposed to the previous case, the pattern

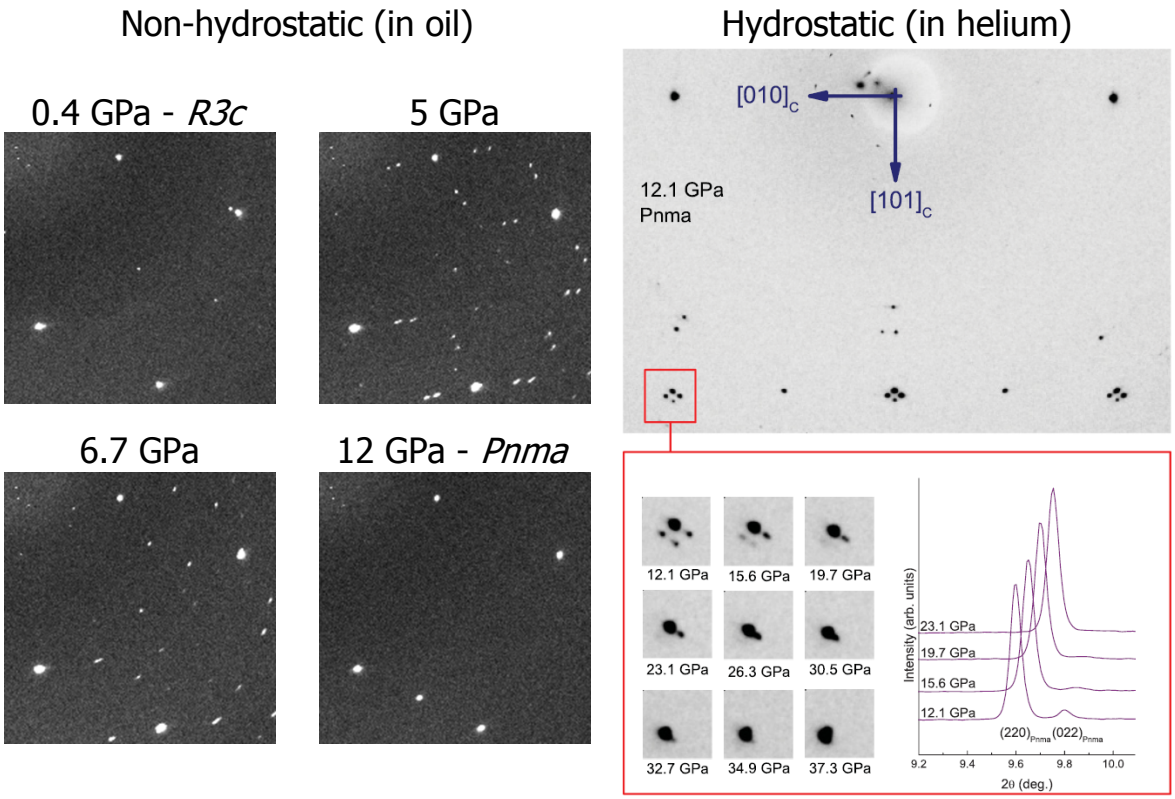

Figure 3.5: Left: Selected area of an integrated diffraction pattern of a $BiFeO_3$ single crystal, measured with silicon oil as pressure transmitting medium. Right: Integrated diffraction pattern in the *Pnma* phase with helium as pressure transmitting medium. The peaks show a splitting associated to the domain structure. The zoom in the red box shows the evolution of the $(222)_C$ reflection under pressure and some corresponding 2θ scans.

shows very clearly the multiple domains. In principle, for a transition $m\bar{3}m \rightarrow mmm$, 6 ferroelastic domains are expected. Only 4 are clearly visible due to the projection. In any case, this shows that the absence of splitting in the previous case has to be attributed to the strongly non-hydrostatic conditions.

As the pressure increases however, the intensity ratios between diffraction spots change. With increasing pressure, some eventually vanish, and a quasi single domain state is formed. This can be understood by the fact that the hydrostaticity is good but never really perfect, and that the duration of the experiment allows the crystal to relax (figure 3.5).

The last two phase transitions at 38 and 48 GPa, in a striking contrast with all the others, do not give rise to the emergence of domains. One hypothesis might be that the slight non-hydrostaticity selects one domain, but the example of $BiMnO_3$ described above, with its remarkable monoclinic domains at 40 GPa in helium, make it sound very unlikely. Instead, the absence of twinning has to be explained by the fact that the transition is not ferroelastic, i.e. does not come with a change of crystal system. This pointed to orthorhombic space groups for the two high-pressure phases.

Symmetry descent and domain formation

Because the number of domains is characteristic of the symmetry descent, it is also possible to gain some information from the presence of domains. A typical example of that situation was found in $BiMnO_3$ [58]. This occurs between 37 and 39 GPa, at the phase transition between the orthorhombic *Pnma* and the "supertetragonal" phase, revealed by the emergence of new peaks in the Raman spectrum and a very clear change in the diffraction pattern. Considering the evolution of the domain structure (figure 3.6), we observe that, before the transition, the crystal undergoes a gradual detwinning similar to the one described above for $BiFeO_3$, and is in a single domain state between 30 and 37 GPa. After the transition, the diffraction pattern shows a (at least) 10-variant ferroelastic domain structure, which can only be expected for a monoclinic or triclinic structure. This simple fact was a strong argument in the determination of possible space groups.

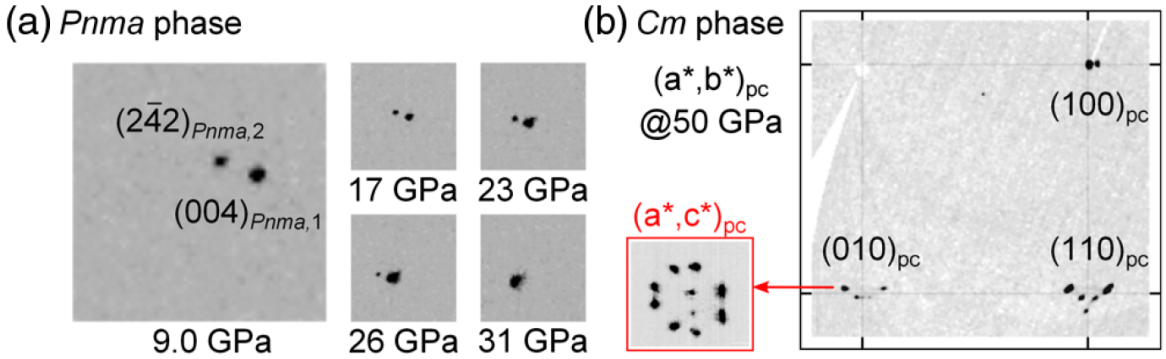

Figure 3.6: (a) Illustration of the detwinning of the $BiMnO_3$ crystal under pressure in the *Pnma* phase; the indices 1 and 2 refer to the two different domains. (b) Selected region of the reciprocal $(a^*, b^*)_{pc}$ plane (pseudo-cubic settings) showing the splittings associated with the domain structure in the *Cm* phase. The zoom shows a map of the $(010)_{pc}$ reflection in the $(a^*, c^*)_{pc}$ plane ($(110) + (001)$ in the monoclinic settings).

4 – Studies of ferroic domain walls

This chapter summarizes results on properties of domain walls. It is more recent, and will be therefore described is some more details. Most of the results shown here were obtained as part of the PhD work of Guillaume Nataf, who defended in October 2016 after 3 years shared between LIST in Luxembourg and the CEA Saclay in France.

4.1 – Context: domain walls as possible functional elements

The previous chapters were dealing with *domain structures*. In this approach, domain walls are merely interfaces separating domains. They are relevant to physical properties, and their contributions may even be dominant, because they move, pin defects or impose specific boundary conditions on the domains, but they have no special properties of their own. These views have changed recently with the realization that domain walls may have properties that differ from the properties of the bulk. The very small size of domain walls, combined with the possibility to create, destroy, move or control them using an appropriate field, has led to a change of paradigm where the wall, rather than the domain, is seen as the functional element in the material [77]. When thought in terms of contrast between bulk and domain walls, it is possible to distinguish several cases.

Conductive walls in insulating bulk: Ferroic oxides as usually insulating. The observation of a contrast in conductivity between the domains and the domain walls is usually traced back to the observation by E. Salje of a superconducting behaviour at ferroelastic domain walls in WO_3. Since then, similar reports has been made in many other cases ($BiFeO_3$, $LiNbO_3$, $ErMnO_3$, PZT...).

Polar walls in non-polar bulk: That compatible ferroelastic walls are polar is a very general symmetry property. In practice, experimental works on polar walls has focused on $SrTiO_3$ and $CaTiO_3$, and experimental evidence is much more scarce than for the previous topic.

Phase transitions within domain walls: This refers to the general idea that a domain wall is a region in space where some order parameter changes sign and, as it passes through zero, enables another competing order parameter to develop, thereby stabilizing a different phase. Probably the most investigated case in ferroelectrics is the possibility of Bloch walls.

The objective of G. Nataf's PhD was to explore experimental methods for experimental studies of domain walls; he concentrated on Raman spectroscopy and low-energy electron microscopy.

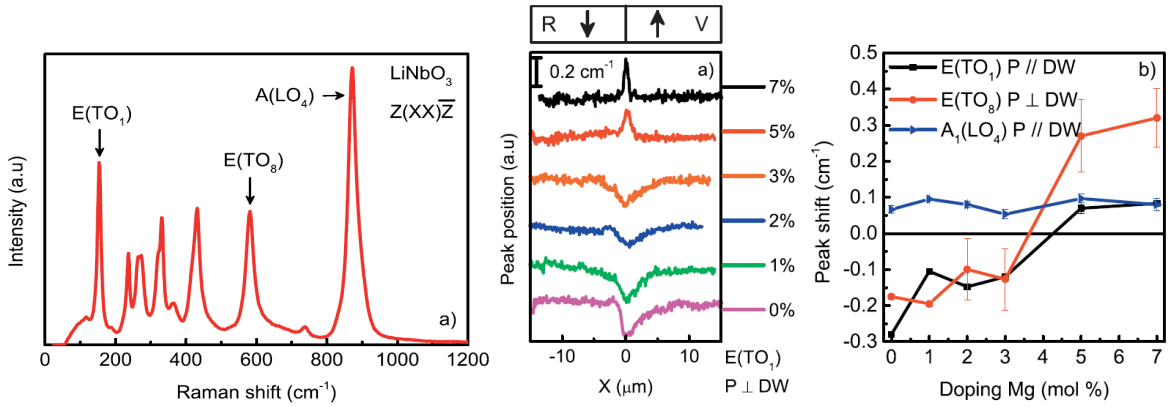

Figure 4.1: (a) Raman spectrum of $LiNbO_3$. The fitted modes are indicated. (b) Peak position of the $E(TO1)$ across a domain wall for different doping concentrations. The curves have been shifted for clarity. The sketch on top indicates the position of the domain wall (V: virgin domain, R: reversed domain). (c) Peak shifts at the domain wall for all peaks and doping concentrations considered. Error bars represent the standard deviation calculated from measurements on three different domain walls. Reproduced from [78]

Let us start with a Raman study of domain walls in Mg-doped $LiNbO_3$. Domain walls in $LiNbO_3$ in general have been extensively studied by Raman spectroscopy [79–84], usually by point-by-point line scans. One reason for this interest is that domains in $LiNbO_3$ are not ferroelastic, so that only 180° domains are found. Both up and down domains have the same Raman spectrum by symmetry, and any contrast observed near the wall can then be attributed to the wall itself. Peak shifts and peak intensity variations of the Raman modes have been observed but their relation to structure remains unclear. They are usually explained by defect concentration differences, or stress induced field variations. The originality of this work was to investigate a number of samples with different dopant concentrations, which allowed us to have a more detailed discussion of the Raman signatures.

A typical Raman spectrum of $LiNbO_3$ in the $z(xx)\bar{z}$ backscattering geometry is shown in Fig. 4.1 (a). As it is usually done, the analysis was done by fitting the spectra in the line scan, and track the positions and widths of the main peaks, as indicated in the figure. The mode frequency for the A_1 mode is shown results for all three modes are summarized in Fig. 4.1 (b). The frequency shift for E(TO1) and E(TO8) at the domain wall is negative below 5% of magnesium but positive above 5%, while it is always positive for A_1(LO4) and nearly independent on the amount of magnesium. The spatial extension of the frequency shifts varies between 0.6 and 6 μm, depending on the amount of magnesium. For samples doped with more than 5 mol% of magnesium, the spatial extension is always below 1.8 μm.

Here, the evolution of the Raman modes for the whole series of Mg concentrations sheds more light on the origin of the frequency shifts. First, it is clear that an intrinsic electric field alone cannot account for all the observations since it would not explain the doping-dependence of the frequency shifts of the E modes. Conversely, a simple picture where the dopant would segregate

at the walls would not be consistent with the observations, notably because the width of E(TO8) and A1(LO4) does not change at the domain wall, whereas they vary strongly in the bulk with variations of Mg content (not shown here). We also rule out a simple mass effect that can be expected upon substitution of Nb by the lighter Mg, since the frequency shift for the A mode shows no doping dependence. Based on this, we propose that both intrinsic fields and defects have to be taken into account. The change in sign of the peak shift at the wall correspond to the change in the dopant incorporation mechanism that is different below and above 5%.

4.3 – Raman spectroscopy at domain walls: methodological investigations

From a methodological point of view, the previous case calls for two comments.

The first comment is simply to highlight that Raman signatures of domain walls can be obtained, in spite of the very small size of the walls compared to the diffraction limit inherent to optical techniques. In micro-Raman spectroscopy, the size of the object is not an issue *per se*, and the resolution limit only means that small objects cannot be resolved, but they may be seen. Carbon nanotubes, graphene and other 2D materials are probably the best examples for this. In the context of domain walls, the challenge is that the signal of the wall is buried into the much stronger signal of the surrounding bulk, because of the difference in volume. Domain walls in $LiNbO_3$ are usually considered to span across a few unit cells at most. Raman spectroscopy, on the other hand, typically probes a volume of the order of 1 μm^3.

The second comment is that the analysis performed in the example above is after all rather unsatisfactory. The choice of Raman peaks in the previous study – like in most studies devoted to $LiNbO_3$ – is based on the possibility to fit the peak with reasonable accuracy, a choice that is merely based on technical feasibility rather than physical relevance. As a result, it does not really allow to fully exploit the information present in the spectra.

In order to move further into a deeper analysis, one option is to go for superresolved techniques, which for Raman could be tip-enhanced Raman spectroscopy (TERS). This was given a try at the beginning of A. Schober PhD at LIST, but it turned out to be too challenging. Still today, very few reports have been published on functional oxides. As an alternative pathway, we have engaged into the statistical analysis of Raman maps and extraction of characteristic signatures at the domain walls. This has motivated some methodological developments and understanding that will be presented in the following.

Raman spectroscopy from a few unit cells: an excursion into ultra-thin films

Before addressing domain walls themselves, this paragraph will make a quick detour through a related experimental problem where statistical treatment of Raman maps have proven fruitful: ultra-thin epitaxial films. This work was performed parallel to the domain wall work during the PhD of A. Schober, as a follow-up of the work done in the group by M. Weber. The films considered here are $LaNiO_3$ films deposited epitaxially on $LaAlO_3$. Both cristallize in the same space group $R\bar{3}c$ corresponding to a tilted perovskite with a $a^-a^-a^-$ tilt system in Glazer's notation, but their tilt angles and lattice parameters are different and $LaNiO_3$ experiences an epitaxial compressive strain of 1.1 % and a strain-induced phase transition from $R\bar{3}c$ to $C2/c$ [22].

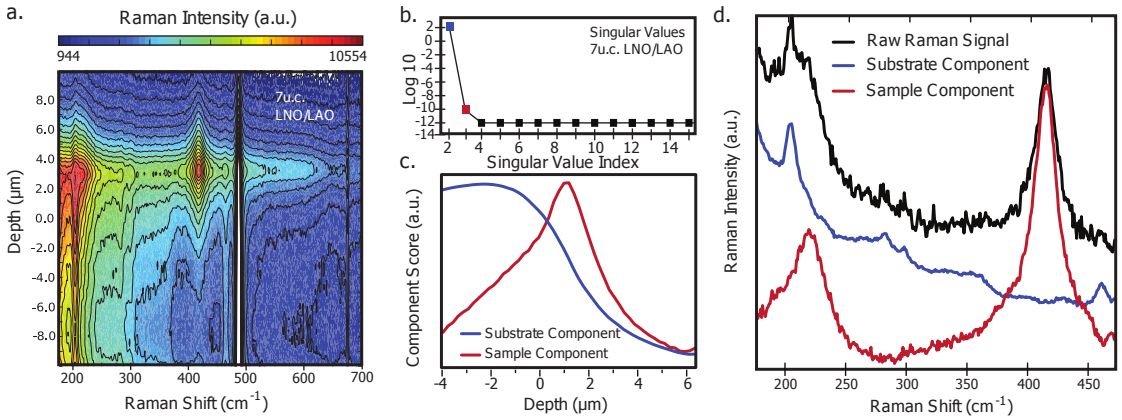

Figure 4.2: Illustration of the analysis of a Raman depth profile by principal component analysis (PCA). (a) Colormap of the dataset as described in the text. (b) Singular values demonstrating that two components only have a significant contribution. (c) Score of the two relevant components. (d) Shapes of the component, here directly identified as the spectrum of the substrate and the film.

The Raman map considered here is depth profile, whereby the sample is moved along the optical axis of the microscope. Fig. 4.2 (a) shows an example of dataset on a film that is 7 unit cells thick (i.e. 2.8 nm). It consists of a collection of 101 spectra acquired with a 0.2 μm step on a 20 μm range. This data set is treated here by principal component analysis (PCA), that allows separating the contributions of the substrate and the film, which is made possible because both signals have different depth dependences. Fig. 4.2 (b–d) shows the outputs of the treatment: the full dataset can be reconstructed from linear combinations of only two components easily assigned to the substrate (larger contribution, step-like depth dependence) and the film (peak-like depth dependence). In this example, the components can be directly identified as the Raman spectra of the substrate and the film. It is however not necessarily the case with the PCA, which is a pure statistical treatment that does not include any physical constraints.

This type of analysis was successfully performed on films as thin as 3 unit cells (1.2 nm), which gives a nice example on how a Raman spectrum can be extracted from a few unit cells of a perovskite oxide on top of a very similar substrate. In the next section, the same method will be applied to domain wall mapping.

Interpretation of principal component analysis of Raman maps

The PCA is a mathematical routine that considers correlations in a dataset, without any consideration for what is physically meaningful. As a result, its output (the components) may not in general be interpreted as Raman spectra. This does not matter for imaging purposes, but it does matter for a more accurate interpretation of the maps. Some other multivariate methods do allow to introduce physically sound constrains in the shape of the components, and have been also explored during A. Schober's work, but will not be discussed further here. When mapping domain walls, we expect small alterations of some reference spectrum, it has been found more profitable to work on the understanding of the component lineshapes given by the PCA. In Ref. [85], we have reported some simulations that give general guidelines that help identify the classical Raman changes: shift

of modes, peak broadening, changes in intensity ratio between peaks. When performed over a full spectrum, this allows to make a quick qualitative assessment of the nature of changes occurring at the wall. Or course, complex spectra with overlapping peaks will make identification trickier.

While PCA is not quantitative, in that it does not directly gives the amplitude of a peak shift, for example, we have shown that it was possible to retrieve and quantify a shift from the PCA results. This was tested for $LiNbO_3$, and gave results essentially similar to the results obtained by conventional peak fitting.

We also studied the influence of noise on the ability to detect small peak shifts. Because PCA is a statistical treatment, it is expected to be affected by the signal-to-noise ratio of the original dataset. It was found that a peak shift of a given amplitude becomes undetectable below some threshold of the signal-to-noise ratio. Conversely, this limits the minimal shifts observable in given measurement conditions.

Principal component analysis on ferroelectric domain walls

With this in mind, let us come back to the case of ferroelectric domain walls in $LiNbO_3$. The sample considered here is again a Z-cut 5 mol% Mg-doped $LiNbO_3$ single crystal. Figure 4.3 shows a PCA on a map of 2x8 μm^2, in 0.1 μm steps, with the first three principal components (PCs) and the corresponding scores. The average spectrum, corresponding to the sum of all the spectra in the data set, is also plotted for reference and can be considered as the typical Raman spectrum of $LiNbO_3$. The number of PCs studied is limited to three because they account for 85% of the total variance. The fourth component accounts for only 0.04% more and contain only noise.

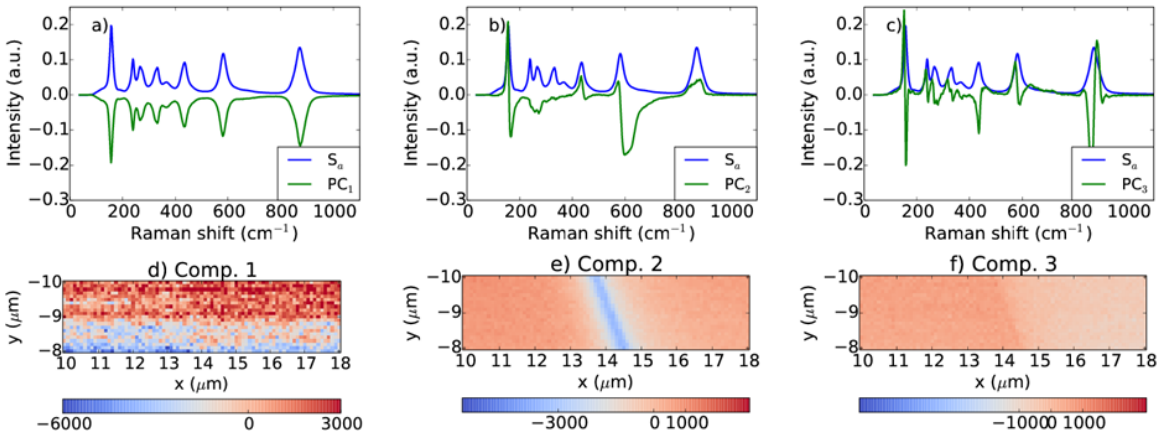

Figure 4.3: Raman maps of ferroelectric domain and domain walls in $LiNbO_3$ analyzed by PCA. The blue spectrum is the average spectrum obtained over the whole map. (a–c) show the first, second and third principal components (green curves) and (d–f) are the corresponding scores.

In Fig. 4.3 (a), the first component is found similar to the average Raman spectrum. By direct comparison with the results of the simulation, this component describes overall changes of intensity of the spectrum. This is due to fluctuations of the laser intensity and drift of the stage during the measurement. The score of this PC is not at all correlated with the position of the domain wall, and it can be simply ignored.

The second component on the other hand clearly shows the position of the wall in its score (Fig. 4.3 (e)) and can directly associated to it. By comparing with simulations, a quick analysis of the main features can me made from the shape of the associated curve. At 154 cm^{-1}, we identify a shift of E(TO1) mode. The intensity variation near 615 cm^{-1} reveals the growing of an additional peak etc.

Interestingly, the score of the third component reveals a small contrast between domains which, by symmetry, is not expected. This contrast originates from a residual internal field due to the poling process. It is explained by the presence of polar defects that do not usually switch with the field, which breaks the symmetry between the two domains. This contrast can be eliminated by annealing the sample, which allows the polar defects to realign with the macroscopic polarization direction.

Principal component analysis of ferroelastic domain walls

Ferroelastic domains have by definition different crystallographic orientations that come with different orientations of the Raman tensor. This creates a contrast in Raman spectroscopy between two adjacent domains. Because of the large size of the laser spot compared to the wall width, the Raman signal at the boundary between two ferroelastic domains contains a weighted average of the different Raman signal from both domains, possibly masking an extra, specific, signature of the DW. Identifying the specific wall signature is therefore much more challenging than in the simple ferroelectric case.

In principle, the Raman contrast between the two domains might cancel out for specific orientation and scattering geometries, as a direct consequence of the strain compatibility condition. In practice though, it may be very difficult to identify and select this geometry. Besides, the cancellation would rely on a perfect realization of Raman selection rules, which are in reality only partly fulfilled because of misorientations, optics, etc.

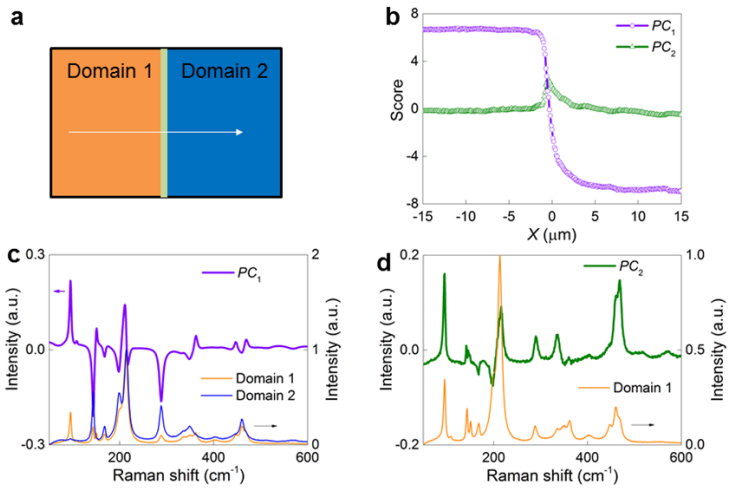

Figure 4.4: PCA of Raman maps of ferroelastic domain and domain walls in $NdGaO_3$. (a) Comparison of PC1 and two spectra from domain 1 and domain 2. (b) Comparison of PC2 with a spectrum from domain 1. (c) Scores of PC1 for every spectrum. (d) Scores of PC2 for every spectrum.

As an example, we investigated $NdGaO_3$, which has *Pnma* structure with 24 Raman active modes, reasonably well identified [86]. Figure 4.4 shows the score of the first component, which clearly maps the ferroelastic domains. The second component on the other hand has nearly zero score in the domains and peaks at the domain walls; it describes an extra contribution observed in the vicinity of the wall. The shape of the component itself indicates that mainly intensity variations of the Raman modes occur at the walls. The detailed interpretation of those changes is a topic for future work, and will most probably require some input for theory. At this stage, we conclude on the possibility to extract signal from ferroelastic domain walls.

4.4 – Studies of polar domain walls in $CaTiO_3$

The polar character of ferroelastic domain walls is a general result derived from symmetry and group theory [4]. Their potential for memory devices has been discussed [87, 88]. In spite of this, they have been less studied experimentally and few examples are known. Most experimental work has been devoted to the perovskites $SrTiO_3$ [89, 90] and $CaTiO_3$ [91, 92]. In $CaTiO_3$, the evidence for the polar character of the wall has been given by TEM and second-harmonic generation.

As a mechanism for domain wall polarity, it has been proposed that one of the octahedra tilts goes to zero at the wall, allowing for the emergence of Ti off-centering and hence polarization, seen as a competing secondary order parameter [93, 94]. A biquadratic coupling between the primary order parameters and polarization is always allowed, and yields two energetically equivalent signs for the wall polarity [95]. On the other hand, strain gradients in the vicinity of walls may induce a strong polarization via linear flexoelectricity and favor a specific polarization direction. Whether or not a domain wall polarization can be switched depends on the respective strengths of these mechanisms.

In our studies of $CaTiO_3$, our concern was to study the polar character of the walls by their electric or dielectric properties, in order to move forward from a pure structural picture to actual material responses that might be used in devices. Two such responses were characterized and reported in Ref. [96].

Macroscopic piezoelectric response of domain walls

The first electric signature is a response of $CaTiO_3$ crystals in a resonant piezoelectric spectroscopy (RPS) experiment done in collaboration with M. Carpenter and E. Salje (Univ. Cambridge). RPS measures characteristic frequencies of mechanical resonances in a sample upon excitation by an AC electric field. Several resonances were observed in the single crystal, with a behaviour with temperature that is consistent with the known elastic properties of $CaTiO_3$. This provides evidence for a piezoelectric response within the material. We attribute this piezoelectric signature to the walls, as previously described for $SrTiO_3$ [90]: the applied ac-field leads to the breathing of polar walls through the piezoelectric effect, creating strain fields around them. The resulting elastic wave becomes resonant at a natural frequency, enhancing considerably the amplitude of the elastic wave.

Two other mechanisms can be invoked to explain the RPS responses in non-ferroelectric phases: (i) polar defects, as in the incipient ferroelectric (non-ferroelastic) $KTaO_3$ and (ii) polar nano-regions as in the cubic phase of $BaTiO_3$ or of $Pb(Sc,Ta)O_3$ [97, 98]. Neither are probable in that case. In the case of $KTaO_3$, above 120 K, the coherence of defect dipoles is low and the RPS signal weak.

With decreasing temperature, switchable defect dipoles freeze in parallel arrangements and induce macroscopic polarity, accompanied by an increase of the piezoelectricity. On the other hand, polar nano-regions and polar defects have not been reported in the literature on $CaTiO_3$. Therefore we conclude that the RPS resonances are indeed induced by polar – and hence piezoelectric âĂŞ-domain walls.

It is interesting to note that the macroscopic piezoelectric response, and hence the RPS signal, should vanish if polar domain walls were statistically perfectly distributed. But this compensation is known to be usually imperfect in piezoelectric materials, and it is very likely that domain walls are distributed unequally, especially considering the comparatively large domain sizes, thereby explaining the existence of the RPS signal.

Low-energy electron microscopy of domain walls

We also looked for evidence of an electric signature of domain walls in $CaTiO_3$ by low-energy electron microscopy (LEEM). This work was done in collaboration with N. Barrett and C. Mathieu at the CEA Saclay. Contrary to RPS, LEEM is a surface technique. The sample was here approximately [111] oriented. Fig. 4.5 (a) shows a topographic image of the area under investigations, where domain walls appear as valleys (V) or ridges (R), depending on the values of strain in both domains. In this area, many different domain wall orientation are present. A precise assignment was attempted, based on the domain wall equations derived from the classical theory of compatible ferroelastic walls, and showed that W and W'-type domain walls are present.

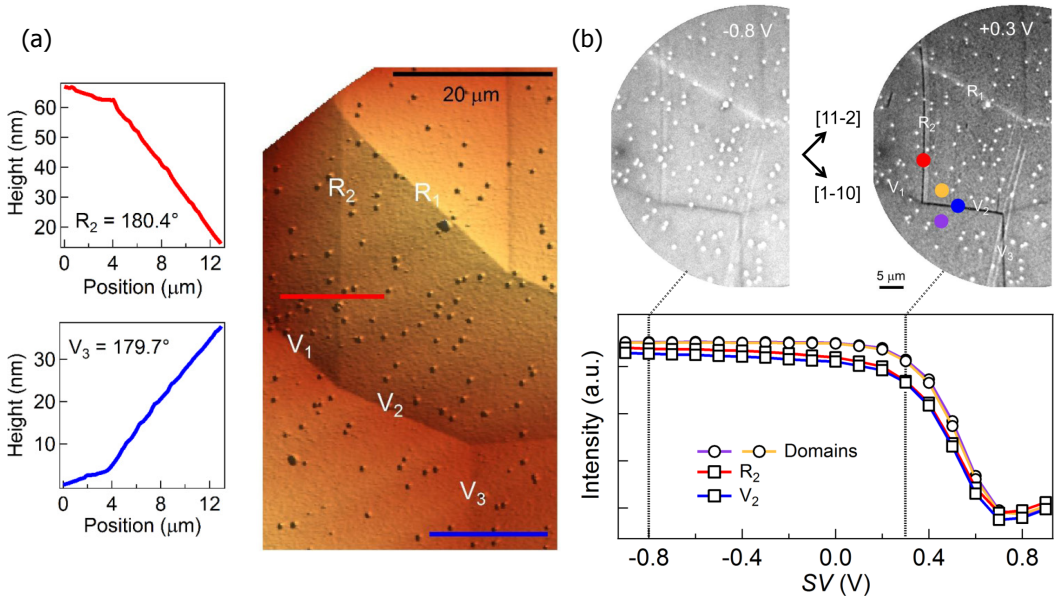

Figure 4.5: (a) AFM topography of the sample surface. Valleys and ridges of the walls are labelled V and R. The upper inset shows the height profile perpendicular to the R_2 ridge, the lower inset the V_3 height profile. (d) MEM images at start voltages of -0.8 and +0.3 V, with the electron intensity as a function of start voltage measured in domains and at R_2 and V_2 showing a 100 mV difference at the MEM-LEEM transition.

The main parameter in a MEM-LEEM experiment is the "start voltage" that determines the kinetic energy of electrons incident on the sample surface. For low start voltages, the kinetic energy is not sufficient for electrons to actually reach the surface and they are reflected and extracted to the analysis column. This is the mirror electron microscopy (MEM) regime. For high start voltages, the electrons penetrate the sample surface and a smaller number of backscattered electrons are extracted to form the image (LEEM regime). The transition between those two regimes is marked by a drop in intensity at some start voltage that is characteristic of the local surface potential.

Fig. 4.5 (b) shows two MEM images taken at start voltages of -0.8 and +0.3 V of the same area as the AFM landscape. In the MEM images the electron intensity from the domain surfaces far away from the walls always has the same value, indicating identical surface potential in all domains. The walls labeled R_2, V_1 ,V_2 and V_3 appear as dark lines whereas R_1 is bright. The electron intensity in the domains and at the walls is also plotted as a function of start voltage. The MEM–LEEM transition occurs at 0.43 V in both domains. At the walls labelled R2 and V2 taken as examples, the MEM–LEEM transition occurs at a start voltage lower by about 100 mV, which is a signature of more positive surface charges at the domain wall with respect to the domains.

Surface topography could be expected to play a role in MEM-LEEM imaging, but it cannot be the dominant origin for the contrast observed here. As shown in Fig. 4.5, ridges R_1 and R_2 have opposite contrasts with respect to surrounding domains. If the contrast was dominated by the physical topography, i.e., by the ridge, it should have the same sign. Since this is not the case, the topography alone cannot account for the contrast. Instead, we claim that it is due to the surface charge induced by the domain wall polarization.

Playing with focusing conditions can be used to enhance the contrast and identify the sign of the out-of-plane polarization. The dark domain walls (R_2, V_1, V_2 and V_3) were found to have outwards pointing, i.e. positive, polarity, whereas R1 has an inward pointing polarity, i.e. negative surface charge. Thus, both ridges and valleys may adopt the same polarity. Conversely, a ridge may have positive or negative polarity.

Having established the signature of domain wall polarization, we proceeded to check if it could be modified. We considered the influence of low energy electron injection on the contrast at the domain walls. Electron injection is accomplished by increasing the start voltage well beyond the MEM-LEEM transition so that the majority of incident electrons penetrate the sample surface. In Figure 4.6, we show MEM images acquired for a start voltage of 0.3 V, following exposure to electrons with a start voltage of 8 V for 2 and 32 minutes, respectively. After 2 minutes the contrast at valleys and at R2 has diminished but has not changed at R_1. After 32 minutes of irradiation, the contrast at R_2 has dropped to zero, it is weaker at valleys, but remains unchanged at R_1. Figure 4.6 shows the quantitative evolution of the contrast with irradiation time for all domain walls. It shows the quite distinct responses of R_1 and R_2 to electron injection, the contrast at R_1 is constant whereas that at R_2 decreases to zero. The contrast at valleys (V_1, V_2 and V_3) is attenuated by about 20% after a 2 minute exposure to the electron beam but then remains constant for longer exposure times. It is possible to recover the initial state of domain wall contrast by annealing the sample above 80°C.

The observation of charge variations associated with domain wall polarization raises the question of a possible ferroelectric, and not only polar, character of the walls. The fact that we observe several type of walls (W and W' types, ridge and valleys) and that they exhibit differences in their MEM contrast suggests that the polarization in the wall can be switched. However, uncertainties in domain wall assignment did not allow us to clearly identify the archetypal situation of opposite

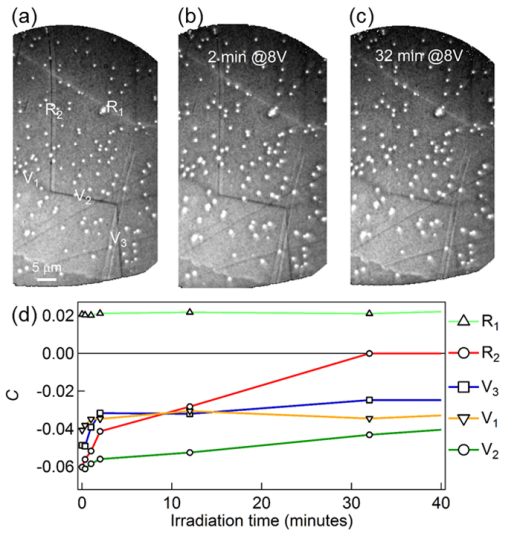

Figure 4.6: Time-dependent MEM images. Images taken at a start voltage of 0.3 V after exposure to 8 V electrons for (a) 0 (b) 2 and (c) 32 minutes. (D) Intensity contrast at the walls as a function of irradiation time.

polarization signs in otherwise strictly identical domain walls, i.e., separating identical domains with the same orientation in space, or conversely, identical polarization charges in opposite walls. Besides, definitive evidence for ferroelectricity, i.e., polarization switching under *electric field*, has yet to be demonstrated. Further investigations are therefore required to conclusively establish the ferroelectric nature of domain walls in $CaTiO_3$.

Part II
From current to future work

5 – Antiferroelectric phase transitions

My studies of antiferroelectric transitions have started some time ago with a collaboration with P. Tolédano during his stay as an invited professor at LIST. The topic has been given a boost recently with the kick-off in September 2017 of a dedicated project and the hiring of a PhD student, Cosme Milesi-Brault, under the joint supervision of E. Defaÿ and myself.

5.1 – Motivations: a relatively neglected material property

The basic picture of antiferroelectric materials (AFEs) was laid down in the original works of Kittel in the 50's, who proposed both a definition (in his seminal textbook) and a phenomenological model of antiferroelectricity [99] that is still invoked as a reference in the field. In this picture, AFEs are seen as analogs of antiferromagnetic materials where spins are replaced with electric dipoles. They are recognized experimentally by three characteristic signatures. At the microscopic scale, the crystal structure contains antiparallel electric dipoles. At the macroscopic scale, the electrical polarization as a function of electric field $P(E)$ shows a characteristic double hysteresis loop revealing the field-induced switching of one sublattice and the associated transition to the polar phase. Last, a transition from a paraelectric to an AFE phase exhibits an anomaly of the dielectric constant. A 1D toy model of an AFE behaviour is sketched in figure 5.1.

However, AFEs constitute a class of materials that is very poorly known when compared to other members of the rich family of ferroelectrics and ferroic materials in general. This is particularly striking in perovskite oxides, where the understanding of the archetypal AFE $PbZrO_3$ remains controversial, with debates on the origin of the AFE behaviour in $PbZrO_3$ in the recent years [100–102]. Other perovskites with AFE properties ($NaNbO_3$, $AgNbO_3$, WO_3) exhibit even more complicated phase diagrams, and been less scrutinized.

The reason for this disaffection is probably twofold. On the one hand, the very definition of antiferroelectricity is not clear. In contrast to ferroelectrics that are recognized by very simple symmetry arguments, no simple argument can tell whether a given crystal structure is AFE or not. The systematic search for new AFE materials is therefore difficult. On the other hand, antiferroelectricity *per se* has not found many uses for practical applications and devices. This again contrasts with ferroelectric materials that are used for decades in transducers, actuators, filters, memories etc.

Altogether, AFE studies seemingly face a chicken-and-egg problem: how to look for applications of something that is not clearly defined? Why bother to clarify a notion that is apparently useless?

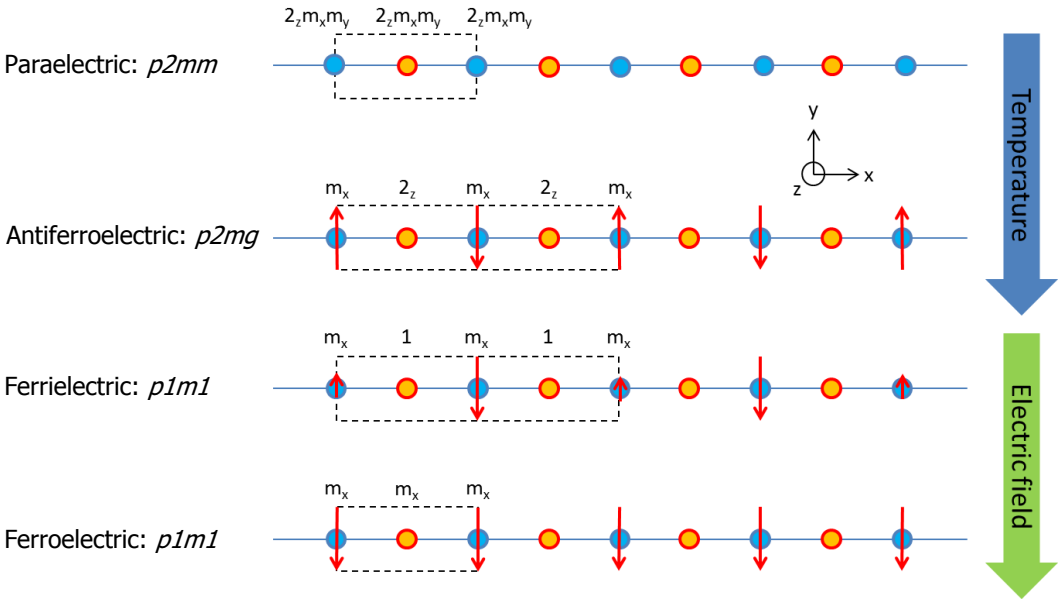

Figure 5.1: Sketch of phase transitions in an elementary 1D antiferroelectric chain. The symbols for symmetries are those of the frieze groups.

The lack of a proper definition for antiferroelectrics is probably the most annoying aspect from an academic point of view. The simple picture of sublattices with opposite polarization works allegedly well in systems where individual electric dipoles can be naturally identified, such as AFE liquid crystals (reviewed in [103]), or some molecular crystals, like KCN where the AFE character is naturally related to the ordering of the dipolar CN^- molecules [104]. However, it breaks down in the general case, and in particular in ferroic oxides with perovskite structures, as soon as dipoles cannot be simply identified nor quantitatively measured. In fact, it has even been strongly argued by major authors in the field that it makes no sense to speak of a "dipolar structure" [105, 106] and that the notion of AFE is at best ill-defined and essentially useless [107, 108]. Those who do not go that far and still find some interest in the notion would agree on the following points [109].

First, what may qualify as antiferroelectric is not a crystal structure, but a phase transition. Systematic search for new AFE materials should therefore be a search for transitions with specific properties, in particular transitions between two non-polar phases with a sharp anomaly of the dielectric constant. Yet, there is so far no commonly accepted criterion to conclusively state whether a given transition is AFE or not. For example, whether or not any ferroelastic transition is potentially AFE remains an open question.

Second, even though the AFE transition itself is between two non-polar phases, a ferroelectric phase should be close in energy, so that it can be stabilized by a strong enough electric field. This is typically examined by first-principles calculations, but only experiment can tell whether this polar phase is achievable or not, and no criterion can tell a priori what is "close enough".

5.2 – Propositions for a theory of antiferroelectric transitions

We have contributed to the AFE problem with two propositions [110]. First, we have proposed symmetry criteria to be fulfilled by AFE transitions that read as follows:

Condition 1: At the PA–AFE transition, a set of crystallographic sites undergo a symmetry lowering that results in the emergence of polar sites and gives rise to a local polarization

Condition 2: The AFE space group has a symmorphic polar subgroup coinciding with the local symmetry of emerging polar sites.

The underlying idea is that the essential phenomemon is a polar transition at the local scale, which does not make it to a polar macroscopic symmetry because of the preservation of some symmetry elements. This approach also gives a prediction for the symmetry of the polar phases, which experimentally remains unknown in most – if not all – cases. As an example, we have predicted AFE properties in $BiVO_4$ and TeO_2, which had so far not been identified as AFE, and found in the literature the corresponding anomaly of the dielectric constant. In fact, those conditions do not appear very restrictive, and it is likely to be verified in a very large number of phase transition. Future will tell whether this approach is fruitful or not.

In a second step, we have put forward a phenomenological model of AFE phase transitions that is different from the classical model by Kittel. The proposed model for the free energy reads:

$$\phi(\eta, P, T) = \phi_0(T) + \frac{\alpha}{2}\eta^2 + \frac{\beta}{4}\eta^4 + \frac{\gamma}{6}\eta^6 + \frac{P^2}{2\chi_0} + \frac{\delta}{2}\eta^2 P^2 - EP \tag{5.1}$$

where η is the primary order parameter for the transition, that need not be related to any sublattice polarization. With this description, a simple AFE material does not exhibit a ferroelectric phase at zero field. Polarization appears only as a secondary order parameter, which only allows the emergence of a polar phase via the mediation of the primary order parameter. This model also reproduces the dielectric anomalies observed at the phase transitions. The phase diagram derived from this model is shown in Fig. 5.2.

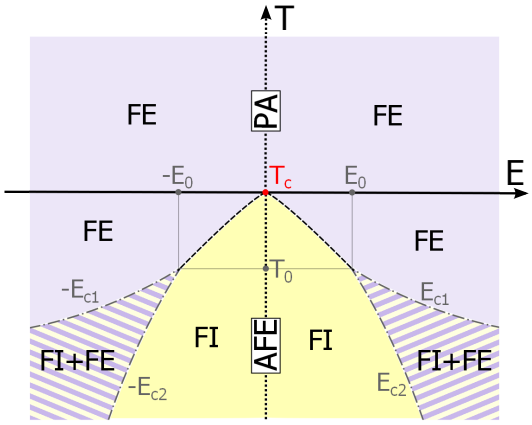

Figure 5.2: Theoretical temperature-electric field phase diagram proposed in Ref. [110]. PA, AFE, FE and FI stand for paraelectric, antiferroelectric, ferroelectric and ferrielectric phases, respectively.

5.3 – Perspectives

The work on AFE is being continued at the moment on a more experimental basis via the project BIAFET (for Bismuth-based antiferroelectrics as tunable materials). This project has been accepted for funding by the Luxembourgish *Fonds national de la recherche* and started in September 2017. Its ambition is to contribute to both ends of the chicken-and-egg problem by working both on the fundamental understanding and the perspectives for applications.

To meet the first objective, we want to contribute to knowledge on antiferroelectricity by studies of the AFE transitions in compounds where the AFE character is so far only loosely known. It is by nature more exploratory and requires to move away from the most classically studied AFEs, in particular perovskites. Two candidates are under scrutiny at the moment. The first is $BiVO_4$, and more generally compounds with the scheelite structure. $BiVO_4$ is particularly appealing because its phase transition occurs at 530 K, and because it is a material that is already intensively studied and synthetized for its photocatalytic properties. The second is the francisite $Cu_3Bi(SeO_3)_2O_2Cl$. In spite of its chemical complexity, this compound it is very appealing because its phase transition is beleived to be a realization of a very simple one-dimensional AFE phase transition, which could make a nice textbook example of the kind.

For the second objective, we want to evaluate the potential of selected AFEs as tunable materials, by measurements of physical properties as a function of electric field across the AFE–FE transition, and to compare this tunability to the state of the art. For that purpose, we plan to focus on materials whose AFE character is well-established: rare-earth doped $BiFeO_3$. Thin films are being synthesized by sol-gel in the composition ranges where the AFE is expected for the different substituents (La, Nd, Sm). We plan to measure the changes in absorption (electrochromic properties) and temperature (electrocaloric properties) at the phase transition.

Beyond this, I am also involved in the project EXPAND (for EXPloring Antiferroelectric oxides as a new technological brick for futur Nanoelectronic Devices). This project involves the Unité mixte CNRS Thalès (E. Bibès, A. Barthélémy), CentraleSupélec (B. Dkhil) and LIST and was launched in January 2018. It focuses on known AFE perovskites ($PbZrO_3$, rare-earth doped $BiFeO_3$) synthesized as epitaxial thin films for applications in nanoelectronics (tunnel junctions, FET). The research focuses on size and interface effects, down to functional characterization of devices.

6 – Electronic and optical properties of ferroelectrics

This chapter will move away from phase transition and address some recent work done on the electronic properties of $BiFeO_3$. This study originated from the will to test ideas on resonant Raman scattering. It is one the main outcome of PhD of Mads Weber, first PhD in our group at LIST and co-supervised by J. Kreisel and myself.

6.1 – Motivations: light-multiferroic interactions

This work is set in a context of a renewed interest for photovoltaic effects in ferroelectrics (or "photoferrolectrics" [111]). $BiFeO_3$ has been studied intensively for its above-band gap photovoltages, anomalous photovoltaic effects, photo-conductive domain walls etc. [112–116]. More recently, the crucial role of in-gap electronic states for the photovoltaic effect has been demonstrated [117]. Yet, the electronic structure in $BiFeO_3$ in general and its band gap in particular, in spite of their importance for photoferroelectric effects, remain rather poorly characterized experimentally, and theoretical works remain scarce and somewhat conflicting. According to absorption studies on single crystals [118] and thin films [119–122], the optical band gap at ambient conditions lies at approximately 2.7 eV. It is also experimentally established that the optical band gap of $BiFeO_3$ shrinks with increasing temperature down to 1.3 eV at 1200 K where it then closes abruptly as a consequence of an insulator-to-metal phase transition [123]. Both this rapid shrinking of the optical band-gap, three times steeper than in $BaTiO_3$ [124], and the insulator-to-metal transition set $BiFeO_3$ apart from conventional non-magnetic ferroelectrics. It is not yet understood how this gradual shrinking of the optical band gap relates to the electronic structure.

One of the reasons for the lack of knowledge is that the experimental investigation of band-to-band transitions is difficult to address experimentally in ferroelectric and multiferroic oxides because the absorption onset is broad, especially when compared to the generally sharp transitions in classical semiconductors. The appearance of Urbach tails at high temperatures complicates the quantitative analysis and the discrimination of direct and indirect transitions. Other classical techniques are rapidly limited by thermal effects, charging of the insulating samples (ARPES). Our approach was to make use of resonant Raman scattering. Resonant Raman scattering happens when the energy of the incident light approaches that of an electronic transition, so that it contains in principle information about the electronic structure.

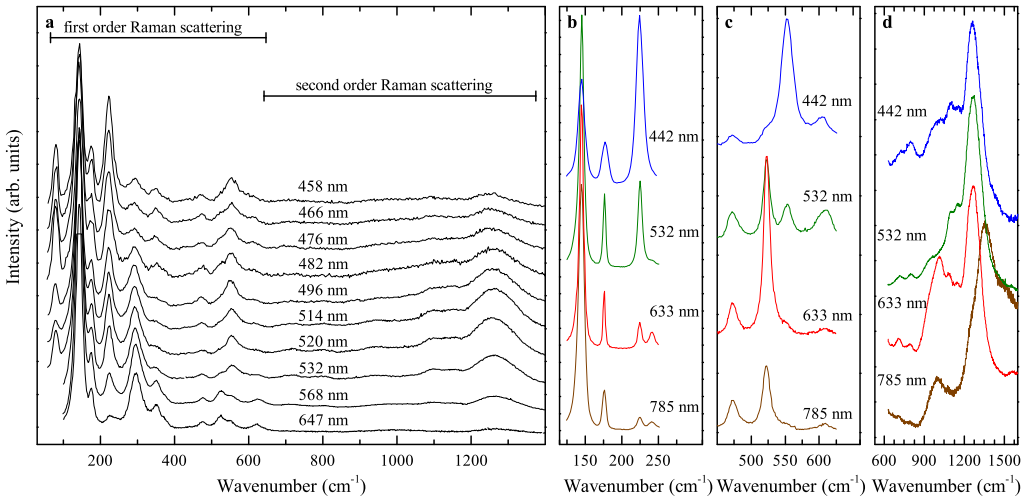

Figure 6.1: a) Raman spectra for different excitation wavelengths ranging from 458 nm to 647 nm. The spectra were recorded at room temperature. For better visibility, the spectra were normalized to the integrated intensity of the first order Raman scattering process. b) and c) Zoom into two low- and high-wavenumber regions. For a better definition of the Raman bands, the spectra were measured at 93 K. d) Second order Raman spectra for several excitation wavelengths at ambient condition.

6.2 – Resonant Raman scattering on $BiFeO_3$

In a first step we have investigated $[001]_{pc}$-oriented $BiFeO_3$ single crystals at room temperature with twelve different excitation wavelengths ranging from 442 nm to 785 nm. Great care was taken to exclude any spurious effect related to crystal orientation, laser polarization, or oblique modes [125], i.e. the orientation of the analyzed domain with respect to the direction of propagation and polarization of the laser was carefully checked in all cases. Fig. 6.1 (a) shows the normalized Raman spectra, which are well defined with sharp bands, especially at lower wavenumbers, and with Raman frequencies in agreement with reported literature data (typically measured with red or green exciting lasers) [125–128]. The most prominent feature of the spectra is that the relative intensity of the different Raman bands greatly depends on the wavelength used. Figures 6.1 (b) and (c) make this more apparent by magnification of two narrow spectral regions: for example, the band at 230 cm^{-1} is very strong at 442 nm but hardly observable at 785 nm; similar changes are observed for almost all modes when carefully considering the full series. The intensity of the second-order Raman spectrum, visible as broad bands in the 1000–1400 cm^{-1} range (see Fig. 6.1 (d)), also depends on the exciting wavelength in agreement with previous reports [129].

Variations of the total intensity and intensity ratios between different bands are characteristic features when passing from non-resonant to resonant Raman scattering. More precisely, resonant Raman scattering is observable only when the Raman scattering process with a particular electronic transition is symmetry-allowed. This situation leads to a divergence of the Raman tensor and a strong enhancement in the Raman scattering signal, where the scattering intensities of the Raman modes are then dominated by the transition probabilities associated to this particular electronic

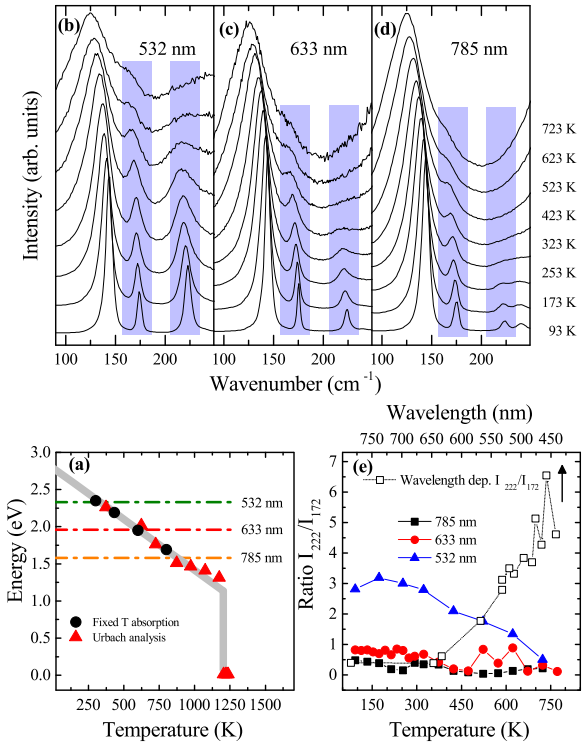

Figure 6.2: (a) Band gap values versus temperature taken from Ref. [123], together with the energies of the 532 nm, 633 nm and 785 nm laser lines. (b)–(d) Temperature-dependent Raman spectra in the low-frequency region for the 532 nm, 633 nm and 785 nm laser lines. The regions in blue highlight two bands that show a significant change in their intensity ratio when crossing resonance (see Figure 6.1 (b)). (e) Evolution of the intensity ratio of the bands located around 172 and 223 cm^{-1} (highlighted in (b)-(d)) with temperature (bottom axis), and with excitation energy at ambient temperature (top axis).

transitions between real – and no longer virtual – electronic states [130, 131]. Because the transition probability differs for each vibrational distortion – and each Raman mode accordingly, the intensity ratios between different modes change with respect to non-resonant situations. In general, not only intrinsic but also defect levels can be involved in this process. Importantly, because first-order Raman scattering is a one-phonon process, only direct electronic transitions can fulfill momentum conservation. In contrast, second-order Raman scattering involves a combination of phonons that may be anywhere in the Brillouin zone, so that second-order resonance processes may involve both direct and indirect interband electronic transitions.

Because changes of the band gaps imply changes in the Raman resonance conditions, resonant Raman spectroscopy can now be used to track its temperature evolution, with the objective to elucidate the rapid shrinking of the optical gap at high temperatures. This principle is illustrated in Figure 6.2 (a), where the band gap values determined by Palai et al. [123] are displayed together with the energies of three selected laser lines used in this study. Strong changes in the resonance conditions are expected when the laser energy is close to the reported band gap, which should be reflected in the intensity and the shape of the Raman signature.

Figure 6.2 (b)–(d) shows the low-frequency part of the first-order Raman spectra for temperatures ranging from 93 K to 773 K and for laser excitation wavelengths 532 nm, 633 nm and 785 nm, i.e. for energies that coincide with the reported band-gap at different temperatures. In all cases, the temperature evolution of the Raman spectra follows a typical behaviour characterized by thermal broadening and a generalized low-frequency shift of all bands with increasing temperature. The intensity ratios between modes do not change significantly compared to the intensity ratio changes observed for different excitation wavelength (see Fig. 6.1). This is quantified in Fig. 6.2 (e) that shows the evolution of the intensity ratio for the two highlighted vibrational bands as an example. This ratio does not show any sign of the dramatic increase that characterizes the resonant regime that would be expected at high temperatures when the laser energy meets the reported optical band gap. This leads to the conclusion that the resonance conditions at a given wavelength do not change with temperature. Considering that only direct electronic transitions can be involved in first-order Raman resonances, we come to the conclusions that the temperature evolution of the optical band-gap cannot be related to a shrinking of a direct electronic band-gap.

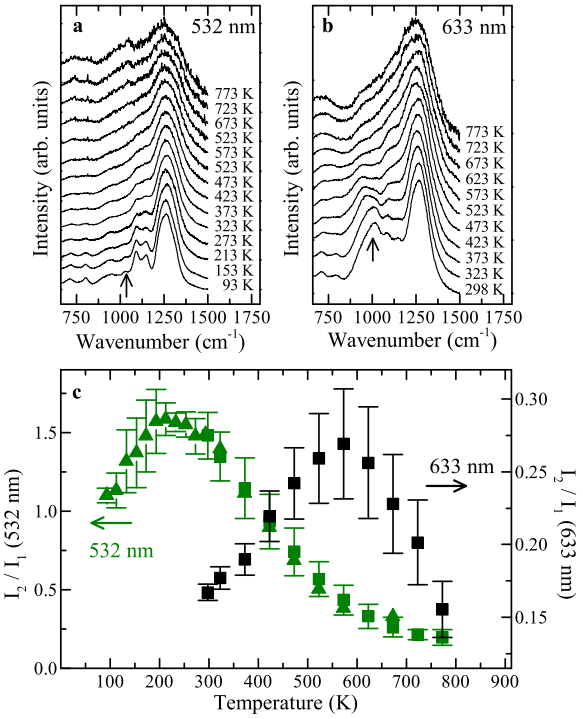

Figure 6.3: a) and b) Temperature-dependent second order Raman spectra under excitation of 633 nm and 532 nm laser light. c) Temperature-dependent ratio of the integrated intensities of the second (I_2) to first order (I_1) Raman scattering spectra.

In a second step, we have scrutinized the second-order Raman spectra. Figures 6.3 (a) and (b) present the temperature evolution of the second-order Raman spectra for excitation of 532 nm and 633 nm. The figures show a strong qualitative change in the intensity signature, which is particularly apparent when comparing the relative intensities of the broad peaks at 1010 and 1260 cm^{-1} under excitation by the 633 nm laser line. The band at 1010 cm^{-1} is strongly reduced at higher temperatures and the shape of the spectrum gradually becomes similar to the spectrum obtained for 532 nm laser at ambient temperature, albeit with differences due to different thermal

broadenings. Conversely, the 532 nm laser line spectra at low temperature revealed a small but distinct band at 1010 cm^{-1} (indicated by the arrow in Figure 6.3 (a) and (b)). These qualitative changes were accompanied by a change in the overall intensity, which we quantify by the ratio between the integrated intensity (I_2) of the second-order spectrum divided by the intensity of the first-order spectrum (I_1). For both excitation wavelengths, I_2/I_1 exhibited a maximum in their temperature dependence. The observed maxima at 573 K for 633 nm and at 223 K for 532 nm retrace the temperature dependence of the reported optical band gap [123]. These changes in shape an intensity of the second-order Raman signature contrasts with the temperature-independent shape of the first-order spectrum. Because any strong change in the energies of direct electronic transitions was ruled out, the observed maxima of the ratio I_2/I_1 can be related to a temperature evolution of an indirect gap. Other possible phenonema are more difficult to reconcile with the experimental observations. Notably, the Franck-condon mechanism explaining the resonance behavior reported in past studies [132, 133] does not have the same signature, both at ambient condition (e.g. no 3^{rd}-order scattering is observed in our studies) and as a function of temperature. Also, a magnetism-related change in the electron-phonon coupling could be admittedly hypothesized from the observation that the maximum for I_2/I_1 at 633 nm lies in the vicinity of T_N, but it is not clear then how to explain the wavelength dependence of this maximum, and the fact that no such anomaly is observed in the vicinity of T_N in the related compound $LaFe_{0.96}Cr_{0.04}O_3$ [133].

Putting together our experimental observations therefore leads to the conclusion that the shrinking of the optical band-gap is related to a temperature-evolution of an electronic band-gap with indirect character. This supports the view that $BiFeO_3$ is an indirect semiconductor, at least above room temperature. On the other hand, the energies of direct electronic transitions show no temperature dependence, which implies in turn non-trivial temperature modifications of the electronic band structure. Even though only hypothesis can be formulated at this stage for the details of this temperature dependence, we note that the hypothesis of a strong electron-phonon coupling inducing an important renormalization of the electronic levels is consistent with the fact that the highest valence band originates predominantly from the oxygen p-states. The low relative mass of the oxygen atom then leads naturally to comparatively large nuclear displacements in the corresponding phonon modes, and hence the largest temperature dependence of oxygen-based bands. Starting from valence and conduction bands considered as nearly flat [123, 134], an increased curvature of the bands at high temperature can explain the different behavior of the direct and indirect gaps.

6.3 – Perspectives

Exciting as it may have been, this work of $BiFeO_3$ has suffered from a number of limitations. First, the lack of knowledge about the changes in absorption with temperature have made corrections impossible and hindered the interpretation of the Raman data. The study also suffered to some extend from the complexity of the Raman spectra of $BiFeO_3$. Because of the very small size of the crystals, measurements had to be done on a $[001]_{pc}$-oriented crystal, i.e. out of the crystallographic axes, which is less than ideal. The theoretical aspect, i.e. the calculation of the resonant Raman spectrum (in collaboration with Xavier Gonze, PhD Yannick Gillet) has been qualitatively very insightful but did not allow to be specific about the electronic levels involved, and direct comparison between theory and experiment was not possible. This has considerably

restricted the interpretations of the Raman observations.

This work will be continued through a PhD to be started in september 2018, with the objective to pursue the work on resonant Raman scattering, and connect with other studies on the photovoltaic effects and electronic structures, notably though photoluminescence and optical measurements. $BiVO_4$, already considered as an potential antiferroelectric material, is also of interest there, due to its strong thermochromism. This will be continued in strong collaboration with the laboratories for photovoltaics at the University of Luxembourg, building on our already fruitful common work.

Bibliography

[1] K. Aizu, *Possible Species of Ferromagnetic, Ferroelectric, and Ferroelastic Crystals*, Phys. Rev. B **2**, 754 (1970).

[2] V. K. Wadhawan, *Introduction to ferroic materials*, Gordon and Breach, Amsterdam, 2000.

[3] J. Sapriel, *Domain-wall orientations in ferroelastics*, Phys. Rev. B **12**, 5128 (1975).

[4] V. Janovec and J. Přívatská, *International Tables for Crystallography*, volume D, chapter 3.4 - Domain structures, pages 449–505, 2006.

[5] A. K. Tagantsev, L. E. Cross, and J. Fousek, *Domains in Ferroic Crystals and Thin Films*, Springer, New York, 2010.

[6] D. Lee, R. K. Behera, P. Wu, H. Xu, Y. L. Li, S. B. Sinnott, S. R. Phillpot, L. Q. Chen, and V. Gopalan, *Mixed Bloch-Néel-Ising character of* 180° *ferroelectric domain walls*, Phys. Rev. B **80**, 060102 (2009).

[7] M. I. Aroyo, D. Orobengoa, G. de la Flor, E. S. Tasci, J. M. Perez-Mato, and H. Wondratschek, *Brillouin-zone database on the Bilbao Crystallographic Server*, Acta Crystallographica Section A **70**, 126 (2014).

[8] H. T. Stokes, D. M. Hatch, and B. J. Campbell, ISOTROPY, 2007.

[9] M. A. Carpenter and C. J. Howard, *Symmetry rules and strain/order-parameter relationships for coupling between octahedral tilting and cooperative Jahn-Teller transitions in* ABX_3 *perovskites. I. Theory*, Acta Cryst. B **65**, 134 (2009).

[10] M. A. Carpenter and C. J. Howard, *Symmetry rules and strain/order-parameter relationships for coupling between octahedral tilting and cooperative Jahn-Teller transitions in* ABX_3 *perovskites. II. Application*, Acta Cryst. B **65**, 147 (2009).

[11] C. J. Howard and M. A. Carpenter, *Octahedral tilting in cation-ordered Jahn–Teller distorted perovskites – a group-theoretical analysis*, Acta Cryst. B **66**, 40 (2010).

[12] D. Orobengoa, C. Capillas, M. I. Aroyo, and J. M. Perez-Mato, *AMPLIMODES: symmetry-mode analysis on the Bilbao Crystallographic Server*, J. Appl. Crystallogr. **42**, 820 (2009).

[13] J. M. Perez-Mato, D. Orobengoa, and M. I. Aroyo, *Mode crystallography of distorted structures*, Acta Crystallographica Section A **66**, 558 (2010).

[14] J. Rodríguez-Carvajal, *Recent advances in magnetic structure determination by neutron powder diffraction*, Physica B: Condensed Matter **192**, 55 (1993).

[15] A. M. Glazer, *The Classification of Tilted Octahedra in Perovskites*, Acta Crystallogr. B **28**, 3384 (1972).

[16] A. M. Glazer, *Simple Ways of Determining Perovskite Structures*, Acta Crystallogr. A **31**, 756 (1975).

[17] P. M. Woodward, *Octahedral Tilting in Perovskites. I. Geometrical Considerations*, Acta Cryst. B **53**, 32 (1997).

[18] P. M. Woodward, *Octahedral Tilting in Perovskites. II. Structure Stabilizing Forces*, Acta Cryst. B **53**, 44 (1997).

[19] K. S. Aleksandrov and J. Bartolomé, *Structural distortions in families of perovskite-like crystals*, Phase Transitions **74**, 255 (2001).

[20] C. J. Howard and H. T. Stokes, *Structures and phase transitions in perovskites – a group-theoretical approach*, Acta Cryst. A **61**, 93 (2005).

[21] R. H. Mitchell, *Perovskites: Modern and ancient*, Almaz Press, Ontario, Canada, 2002.

[22] M. C. Weber, M. Guennou, N. Dix, D. Pesquera, F. Sánchez, G. Herranz, J. Fontcuberta, L. López-Conesa, S. Estradé, F. Peiró, J. Íñiguez, and J. Kreisel, *Multiple strain-induced phase transitions in* $LaNiO_3$ *thin films*, Phys. Rev. B **94**, 014118 (2016).

[23] R. Vilarinho, D. J. Passos, E. C. Queirós, P. B. Tavares, A. Almeida, M. C. Weber, M. Guennou, J. Kreisel, and J. Agostinho Moreira, *Suppression of cooperative Jahn-Teller distortion and its effect on Raman octahedra rotation modes of* $TbMn_{1-x}Fe_xO_3$, Phys. Rev. B **97**, 144110 (2018).

[24] M. N. Iliev, M. V. Abrashev, J. Laverdière, S. Jandl, M. M. Gospodinov, Y.-Q. Wang, and Y.-Y. Sun, *Distortion-dependent Raman spectra and mode mixing in* $RMnO_3$ *perovskites (R = La,Pr,Nd,Sm,Eu,Gd,Tb,Dy,Ho,Y)*, Phys. Rev. B **73**, 064302 (2006).

[25] N. D. Todorov, M. V. Abrashev, and V. G. Ivanov, *Frequency dependence of the quasi-soft Raman-active modes in rotationally distorted* $R^{3+}B^{3+}O_3$ *perovskites (*R^{3+} *= rare earth,* B^{3+} *= Al, Sc, Ti, V, Cr, Mn, Fe, Co, Ni, Ga)*, J. Phys.: Condens. Matter **24**, 175404 (2012).

[26] J. J. Lima-Silva, I. Guedes, J. Mendes Filho, A. P. Ayala, M. H. Lente, J. A. Eiras, and D. Garcia, *Phase diagram of the relaxor* $(1-x)Pb(Zn_{1/3}Nb_{2/3})O_3$-$xPbTiO_3$ *investigated by dielectric and Raman spectroscopies*, Solid State Commun. **131**, 111 (2004).

[27] J. Rödel, *Effective intrinsic linear properties of laminar piezoelectric composites and simple ferroelectric domain structures*, Mechanics of Materials **39**, 302 (2007).

[28] M. Guennou, H. Dammak, P. Djémia, P. Moch, and M. Pham-Thi, *Electromechanical properties of single domain PZN-12%PT measured by three different methods*, Solid State Sciences **12**, 298 (2009).

[29] M. Guennou, H. Dammak, and M. P. Thi, *2T domain-engineered piezoelectric single crystals: Calculations and application to PZN-12%PT poled along [101]*, Journal of Applied Physics **104**, 074102 (2008).

[30] W. Cao, S. Zhu, and B. Jiang, *Analysis of shear modes in a piezoelectric vibrator*, J. Appl. Phys. **83**, 4415 (1998).

[31] M. Davis, M. Budimir, D. Damjanovic, and N. Setter, *Rotator and extender ferroelectrics: Importance of the shear coefficient to the piezoelectric properties of domain-engineered crystals and ceramics*, J. Appl. Phys. **101**, 054112 (2007).

[32] M. Guennou, M. Savinov, J. Drahokoupil, H. Luo, and J. Hlinka, *Piezoelectric properties of tetragonal single-domain Mn-doped NBT-6%BT single crystals*, Appl. Phys. A **116**, 225 (2014).

[33] S. Wada and T. Tsurumi, *Enhanced piezoelectricity of barium titanate single crystals with engineered domain configuration*, British Ceramic Transactions **103**, 93 (2004).

[34] S. Wada, K. Muraoka, H. Kakemoto, T. Tsurumi, and H. Kumagai, *Preparation of Potassium Niobate Crystals with Fine Engineered Domain Configurations and Their Enhanced Piezoelectric Properties*, Ferroelectrics **319**, 127 (2005).

[35] S. Wada, K. Muraoka, H. Kakemoto, T. Tsurumi, and H. Kumagai, *Enhanced piezoelectric properties of potassium niobate single crystals with fine engineered domain configurations*, Materials Science and Engineering: B **120**, 186 (2005).

[36] S. Wada, K. Yako, H. Kakemoto, T. Tsurumi, and T. Kiguchi, *Enhanced piezoelectric properties of barium titanate single crystals with different engineered-domain sizes*, J. Appl. Phys. **98**, 014109 (2005).

[37] K. Yako, H. Kakemoto, T. Tsurumi, and S. Wada, *Domain size dependence of d_{33} piezoelectric properties for barium titanate single crystals with engineered domain configurations*, Materials Science and Engineering B **120**, 181 (2005).

[38] P. Ondrejkovic, P. Marton, M. Guennou, N. Setter, and J. Hlinka, *Piezoelectric properties of twinned ferroelectric perovskites with head-to-head and tail-to-tail domain walls*, Phys. Rev. B **88**, 024114 (2013).

[39] M. Guennou, P. Bouvier, J. Kreisel, and D. Machon, *Pressure-temperature phase diagram of $SrTiO_3$ up to 53 GPa*, Phys. Rev. B **81**, 054115 (2010).

[40] P. Bouvier and J. Kreisel, *Pressure-induced phase transition in $LaAlO_3$*, J. Phys.: Condens. Matter **14**, 3981 (2002).

[41] R. J. Angel, J. Zhao, and N. L. Ross, *General Rules for Predicting Phase Transitions in Perovskites due to Octahedral Tilting*, Phys. Rev. Lett. **95**, 025503 (2005).

[42] H. J. Xiang, M. Guennou, J. Íñiguez, J. Kreisel, and L. Bellaiche, *Rules and mechanisms governing octahedral tilts in perovskites under pressure*, Phys. Rev. B **96**, 054102 (2017).

[43] M. Guennou, P. Bouvier, G. Garbarino, and J. Kreisel, *Structural investigation of $LaAlO_3$ up to 63 GPa*, J. Phys.: Condens. Matter **23**, 395401 (2011).

[44] M. Guennou, P. Bouvier, B. Krikler, J. Kreisel, R. Haumont, and G. Garbarino, *High-pressure investigation of $CaTiO_3$ up to 60 GPa using x-ray diffraction and Raman spectroscopy*, Phys. Rev. B **82**, 134101 (2010).

[45] E. K. H. Salje, M. Guennou, P. Bouvier, M. A. Carpenter, and J. Kreisel, *High pressure ferroelastic phase transition in $SrTiO_3$*, J. Phys.: Condens. Matter **23**, 275901 (2011).

[46] A. Tröster, W. Schranz, and R. Miletich, *How to Couple Landau Theory to an Equation of State*, Phys. Rev. Lett. **88**, 055503 (2002).

[47] W. Schranz, A. Troster, J. Koppensteiner, and R. Miletich, *Finite strain Landau theory of high pressure phase transformations*, J. Phys.: Condens. Matter **19**, 275202 (2007).

[48] A. Tröster, W. Schranz, F. Karsai, and P. Blaha, *Fully Consistent Finite-Strain Landau Theory for High-Pressure Phase Transitions*, Phys. Rev. X **4**, 031010 (2014).

[49] M. Guennou, P. Bouvier, G. Garbarino, J. Kreisel, and E. K. H. Salje, *Pressure-induced phase transition(s) in $KMnF_3$ and the importance of the excess volume for phase transitions in perovskite structures*, J. Phys.: Condens. Matter **23**, 485901 (2011).

[50] U. D. Venkateswaran, V. M. Naik, and R. Naik, *High-pressure Raman studies of polycrystalline $BaTiO_3$*, Phys. Rev. B **58**, 14256 (1998).

[51] A. Sani, M. Hanfland, and D. Levy, *Pressure and Temperature Dependence of the Ferroelectric-Paraelectric Phase Transition in $PbTiO_3$*, J. Solid State Chem. **167**, 446 (2002).

[52] D. Gourdain, P. Pruzan, J. M. Besson, S. Klotz, J. C. Chervin, B. Canny, W. G. Marshall, J. S. Loveday, and M. Hanfland, *Compression of $KNbO_3$ up to 30 GPa: Transition sequence orthorhombic–tetragonal–cubic*, Phys. Rev. B **65**, 054104 (2002).

[53] P. Pruzan, D. Gourdain, and J. C. Chervin, *Vibrational dynamics and phase diagram of $KNbO_3$ up to 30 GPa and from 20 to 500 K*, Phase Transitions **80**, 1103 (2007).

[54] I. A. Kornev, L. Bellaiche, P. Bouvier, P.-E. Janolin, B. Dkhil, and J. Kreisel, *Ferroelectricity of Perovskites under Pressure*, Phys. Rev. Lett. **95**, 196804 (2005).

[55] I. A. Kornev and L. Bellaiche, *The nature of ferroelectricity under pressure*, Phase Transitions **80**, 385 (2007).

[56] P.-E. Janolin, P. Bouvier, J. Kreisel, P. A. Thomas, I. A. Kornev, L. Bellaiche, W. Crichton, M. Hanfland, and B. Dkhil, *High-Pressure Effect on $PbTiO_3$: An Investigation by Raman and X-Ray Scattering up to 63 GPa*, Phys. Rev. Lett. **101**, 237601 (2008).

[57] S. Tyagi, G. Sharma, and V. G. Sathe, *Competition and coexistence of polar and non-polar states in $Sr_{1-x}Ca_xTiO_3$: an investigation using pressure dependent Raman spectroscopy*, J. Phys.: Condens. Matter **30**, 105401 (2018).

[58] M. Guennou, P. Bouvier, P. Toulemonde, C. Darie, C. Goujon, P. Bordet, M. Hanfland, and J. Kreisel, *Jahn-Teller, Polarity, and Insulator-to-Metal Transition in $BiMnO_3$ at High Pressure*, Phys. Rev. Lett. **112**, 075501 (2014).

[59] M. Guennou, M. Viret, and J. Kreisel, *Bismuth-based perovskites as multiferroics*, C. R. Phys. **16**, 182 (2015).

[60] J.-S. Zhou, J. Alonso, J. Han, M. Fernandez-Diaz, J.-G. Cheng, and J. Goodenough, *Jahn-Teller distortion in perovskite $KCuF_3$ under high pressure*, J. Fluorine Chem. **132**, 1117 (2011).

[61] I. Loa, P. Adler, A. Grzechnik, K. Syassen, U. Schwarz, M. Hanfland, G. K. Rozenberg, P. Gorodetsky, and M. P. Pasternak, *Pressure-Induced Quenching of the Jahn-Teller Distortion and Insulator-to-Metal Transition in* $LaMnO_3$, Phys. Rev. Lett. **87**, 125501 (2001).

[62] D. A. Mota, A. Almeida, V. H. Rodrigues, M. M. R. Costa, P. Tavares, P. Bouvier, M. Guennou, J. Kreisel, and J. A. Moreira, *Dynamic and structural properties of orthorhombic rare-earth manganites under high pressure*, Phys. Rev. B **90**, 054104 (2014).

[63] J. Oliveira, J. Agostinho Moreira, A. Almeida, V. H. Rodrigues, M. M. R. Costa, P. B. Tavares, P. Bouvier, M. Guennou, and J. Kreisel, *Structural and insulator-to-metal phase transition at 50 GPa in $GdMnO_3$*, Phys. Rev. B **85**, 052101 (2012).

[64] O. Diéguez, O. E. González-Vázquez, J. C. Wojdeł, and J. Íñiguez, *First-principles predictions of low-energy phases of multiferroic $BiFeO_3$*, Phys. Rev. B **83**, 094105 (2011).

[65] M. Guennou, P. Bouvier, G. S. Chen, B. Dkhil, R. Haumont, G. Garbarino, and J. Kreisel, *Multiple high-pressure phase transitions in $BiFeO_3$*, Phys. Rev. B **84**, 174107 (2011).

[66] M. Guennou, P. Bouvier, R. Haumont, G. Garbarino, and J. Kreisel, *High-pressure phase transitions in $BiFeO_3$: hydrostatic vs. non-hydrostatic conditions*, Phase Transitions **84**, 474 (2011).

[67] R. Haumont, P. Bouvier, A. Pashkin, K. Rabia, S. Frank, B. Dkhil, W. A. Crichton, C. A. Kuntscher, and J. Kreisel, *Effect of high pressure on multiferroic $BiFeO_3$*, Phys. Rev. B **79**, 184110 (2009).

[68] D. P. Kozlenko, A. A. Belik, A. V. Belushkin, E. V. Lukin, W. G. Marshall, B. N. Savenko, and E. Takayama-Muromachi, *Antipolar phase in multiferroic $BiFeO_3$ at high pressure*, Phys. Rev. B **84**, 094108 (2011).

[69] S. Prosandeev, D. Wang, W. Ren, J. Íñiguez, and L. Bellaiche, *Novel Nanoscale Twinned Phases in Perovskite Oxides*, Adv. Funct. Mater. **23**, 234 (2013).

[70] A. Gavriliuk, V. Struzhkin, I. Lyubutin, M. Hu, and H. Mao, *Phase transition with suppression of magnetism in BiFeO3 at high pressure*, JETP Lett. **82**, 224 (2005).

[71] A. G. Gavriliuk, V. V. Struzhkin, I. S. Lyubutin, and I. A. Troyan, *Equation of State and Structural Transition at High Hydrostatic Pressures in the $BiFeO_3$ Crystal*, JETP Lett. **86**, 197 (2007).

[72] A. G. Gavriliuk, V. V. Struzhkin, I. S. Lyubutin, S. G. Ovchinnikov, M. Y. Hu, and P. Chow, *Another mechanism for the insulator-metal transition observed in Mott insulators*, Phys. Rev. B **77**, 155112 (2008).

[73] A. Friedrich, *The effects of extreme pressures on single-crystal structures with distortions of the cation coordination sphere*, High Pressure Research **33**, 523 (2013).

[74] D. C. Arnold, K. S. Knight, G. Catalan, S. A. T. Redfern, J. F. Scott, P. Lightfoot, and F. D. Morrison, *The β-to-γ Transition in $BiFeO_3$: A Powder Neutron Diffraction Study*, Adv. Funct. Mater. **20**, 2116 (2010).

[75] J. Fuksa and V. Janovec, *Which Engineered Domain Structures Can be Produced by External Fields?*, Ferroelectrics **292**, 37 (2003).

[76] S. Klotz, J. Chervin, P. Munsch, and G. Le Marchand, *Hydrostatic limits of 11 pressure transmitting media*, J. Phys. D: Appl. Phys. **42**, 075413 (2009).

[77] G. Catalan and J. F. Scott, *Physics and Applications of Bismuth Ferrite*, Adv. Mater. **21**, 2463 (2009).

[78] G. F. Nataf, M. Guennou, A. Hauß mann, N. Barrett, and J. Kreisel, *Evolution of defect signatures at ferroelectric domain walls in Mg-doped $LiNbO_3$*, Phys. Status Solidi RRL **10**, 222 (2016).

[79] M. D. Fontana, R. Hammoum, P. Bourson, S. Margueron, and V. Y. Shur, *Raman Probe on PPLN Microstructures*, Ferroelectrics **373**, 26 (2008).

[80] G. Stone and V. Dierolf, *Influence of ferroelectric domain walls on the Raman scattering process in lithium tantalate and niobate*, Opt. Lett. **37**, 1032 (2012).

[81] G. Stone, D. Lee, H. Xu, S. R. Phillpot, and V. Dierolf, *Local probing of the interaction between intrinsic defects and ferroelectric domain walls in lithium niobate*, Appl. Phys. Lett. **102**, 042905 (2013).

[82] Y. Kong, J. Xu, B. Li, S. Chen, Z. Huang, L. Zhang, S. Liu, W. Yan, H. Liu, X. Xie, L. Shi, X. Li, and G. Zhang, *The asymmetry between the domain walls of periodically poled lithium niobate crystals*, Optical Materials **27**, 471 (2004).

[83] L. Mateos, L. E. Bausá, and M. O. Ramírez, *Micro-spectroscopic characterization of ferroelectric domain structures in Yb^{3+}:$LiNbO_3$ prepared by electron beam writing*, Opt. Mater. Express **4**, 1077 (2014).

[84] A. Boes, V. Sivan, G. Ren, D. Yudistira, S. Mailis, E. Soergel, and A. Mitchell, *Precise, reproducible nano-domain engineering in lithium niobate crystals*, Appl. Phys. Lett. **107**, 022901 (2015).

[85] G. F. Nataf, N. Barrett, J. Kreisel, and M. Guennou, *Raman Signatures of Ferroic Domain Walls captured by Principal Component Analysis*, J. Phys.: Condens. Matter **30**, 035902 (2017).

[86] O. Kamishima, H. Koyama, R. Takahashi, Y. Abe, T. Sato, and T. Hattori, *Raman study on symmetry analysis in $NdGaO_3$*, J. Phys.: Condens. Matter **14**, 3905 (2002).

[87] E. K. H. Salje and J. F. Scott, *Ferroelectric Bloch-line switching: A paradigm for memory devices?*, Appl. Phys. Lett. **105**, 252904 (2014).

[88] E. Salje and H. Zhang, *Domain boundary engineering*, Phase Transitions **82**, 452 (2009).

[89] J. F. Scott, E. K. H. Salje, and M. A. Carpenter, *Domain Wall Damping and Elastic Softening in $SrTiO_3$: Evidence for Polar Twin Walls*, Phys. Rev. Lett. **109**, 187601 (2012).

[90] E. K. H. Salje, O. Aktas, M. A. Carpenter, V. V. Laguta, and J. F. Scott, *Domains within Domains and Walls within Walls: Evidence for Polar Domains in Cryogenic $SrTiO_3$*, Phys. Rev. Lett. **111**, 247603 (2013).

[91] S. Van Aert, S. Turner, R. Delville, D. Schryvers, G. Van Tendeloo, and S. E. K. H, *Direct Observation of Ferrielectricity at Ferroelastic Domain Boundaries in $CaTiO_3$ by Electron Microscopy*, Adv. Mater. **24**, 523 (2012).

[92] H. Yokota, H. Usami, R. Haumont, P. Hicher, J. Kaneshiro, E. K. H. Salje, and Y. Uesu, *Direct evidence of polar nature of ferroelastic twin boundaries in* $CaTiO_3$ *obtained by second harmonic generation microscope*, Phys. Rev. B **89**, 144109 (2014).

[93] W. Lee, E. Salje, and U. Bismayer, *Structure and Transport Properties of Ferroelastic Domain Walls in a Simple Model*, Phase Transitions **76**, 81 (2003).

[94] L. Goncalves-Ferreira, S. A. T. Redfern, E. Artacho, and E. K. H. Salje, *Ferrielectric Twin Walls in $CaTiO_3$*, Phys. Rev. Lett. **101**, 097602 (2008).

[95] E. K. H. Salje, S. Li, M. Stengel, P. Gumbsch, and X. Ding, *Flexoelectricity and the polarity of complex ferroelastic twin patterns*, Phys. Rev. B **94**, 024114 (2016).

[96] G. F. Nataf, M. Guennou, J. Kreisel, P. Hicher, R. Haumont, O. Aktas, E. K. H. Salje, L. Tortech, C. Mathieu, D. Martinotti, and N. Barrett, *Control of surface potential at polar domain walls in a nonpolar oxide*, Phys. Rev. Materials **1**, 074410 (2017).

[97] O. Aktas, E. K. H. Salje, S. Crossley, G. I. Lampronti, R. W. Whatmore, N. D. Mathur, and M. A. Carpenter, *Ferroelectric precursor behavior in $PbSc_{0.5}Ta_{0.5}O_3$ detected by field-induced resonant piezoelectric spectroscopy*, Phys. Rev. B **88**, 174112 (2013).

[98] O. Aktas, M. A. Carpenter, and E. K. H. Salje, *Polar precursor ordering in $BaTiO_3$ detected by resonant piezoelectric spectroscopy*, Appl. Phys. Lett. **103**, 142902 (2013).

[99] C. Kittel, *Theory of Antiferroelectric Crystals*, Phys. Rev. **82**, 729 (1951).

[100] A. K. Tagantsev, K. Vaideeswaran, S. B. Vakhrushev, A. V. Filimonov, R. G. Burkovsky, A. Shaganov, D. Andronikova, A. I. Rudskoy, A. Q. R. Baron, H. Uchiyama, D. Chernyshov, A. Bosak, Z. Ujma, K. Roleder, A. Majchrowski, J.-H. Ko, and N. Setter, *The origin of antiferroelectricity in $PbZrO_3$*, Nat. Commun. **4**, 2229 (2013).

[101] J. Hlinka, T. Ostapchuk, E. Buixaderas, C. Kadlec, P. Kuzel, I. Gregora, J. Kroupa, M. Savinov, A. Klic, J. Drahokoupil, I. Etxebarria, and J. Dec, *Multiple Soft-Mode Vibrations of Lead Zirconate*, Phys. Rev. Lett. **112**, 197601 (2014).

[102] J. Íñiguez, M. Stengel, S. Prosandeev, and L. Bellaiche, *First-principles study of the multimode antiferroelectric transition in* $PbZrO_3$, Phys. Rev. B **90**, 220103 (2014).

[103] H. Takezoe, E. Gorecka, and M. Čepič, *Antiferroelectric liquid crystals: Interplay of simplicity and complexity*, Reviews of Modern Physics **82**, 897 (2010).

[104] H. T. Stokes and D. M. Hatch, *Model for the ordered phases in KCN and NaCN*, Phys. Rev. B **30**, 3845 (1984).

[105] L. D. Landau and E. M. Lifshitz, *Electrodynamics of Continuous Media*, 1960.

[106] A. P. Levanyuk and D. G. Sannikov, *Anomalies in dielectric properties in phase transitions*, Soviet Physics JETP **28**, 134 (1969).

[107] J. Roos, R. Kind, and J. Petzelt, *Phase Transitions and Lattice Dynamics in $Ag_2H_3IO_6$ and $(NH_4)_2H_3IO_6$*, Z. Physik B **24**, 99 (1976).

[108] J. F. Scott, *Soft-mode spectroscopy. Experimental studies of structural phase transitions*, Reviews of Modern Physics **46**, 83 (1974).

[109] K. M. Rabe, *Functional Metal Oxides: New Science and Novel Applications*, Wiley, 2013.

[110] P. Tolédano and M. Guennou, *Theory of antiferroelectric phase transitions*, Phys. Rev. B **94**, 014107 (2016).

[111] V. M. Fridkin, *Photoferroelectrics*, Springer-Verlag, Berlin Heidelberg, 1979.

[112] S. Y. Yang, J. Seidel, B. S. J., S. P., Y. C.-H., M. D. Rossell, P. Yu, Y.-H. Chu, S. J. F., A. J. W., M. L. W., and R. R., *Above-bandgap voltages from ferroelectric photovoltaic devices*, Nat Nano **5**, 143 (2010).

[113] M. Alexe and D. Hesse, *Tip-enhanced photovoltaic effects in bismuth ferrite*, Nat Commun **2**, 256 (2011).

[114] J. Seidel, D. Fu, S.-Y. Yang, E. Alarcón-Lladó, J. Wu, R. Ramesh, and J. W. Ager, *Efficient Photovoltaic Current Generation at Ferroelectric Domain Walls*, Phys. Rev. Lett. **107**, 126805 (2011).

[115] B. Kundys, M. Viret, D. Colson, and D. O. Kundys, *Light-induced size changes in $BiFeO_3$ crystals*, Nat. Mater. **9**, 803 (2010).

[116] A. Bhatnagar, A. Roy Chaudhuri, Y. Heon Kim, D. Hesse, and M. Alexe, *Role of domain walls in the abnormal photovoltaic effect in $BiFeO_3$*, Nat Commun **4**, (2013).

[117] M. Yang, A. Bhatnagar, and M. Alexe, *Electronic Origin and Tailoring of Photovoltaic Effect in $BiFeO_3$ Single Crystals*, Adv. Electron. Mater. , in print (2015).

[118] X. S. Xu, T. V. Brinzari, S. Lee, Y. H. Chu, L. W. Martin, A. Kumar, S. McGill, R. C. Rai, R. Ramesh, V. Gopalan, S. W. Cheong, and J. L. Musfeldt, *Optical properties and magnetochromism in multiferroic $BiFeO_3$*, Phys. Rev. B **79**, 134425 (2009).

[119] S. R. Basu, L. W. Martin, Y. H. Chu, M. Gajek, R. Ramesh, R. C. Rai, X. Xu, and J. L. Musfeldt, *Photoconductivity in $BiFeO_3$ thin films*, Appl. Phys. Lett. **92**, 091905 (2008).

[120] J. F. Ihlefeld, N. J. Podraza, Z. K. Liu, R. C. Rai, X. Xu, T. Heeg, Y. B. Chen, J. Li, R. W. Collins, J. L. Musfeldt, X. Q. Pan, J. Schubert, R. Ramesh, and D. G. Schlom, *Optical band gap of $BiFeO_3$ grown by molecular-beam epitaxy*, Appl. Phys. Lett. **92**, 142908 (2008).

[121] A. Kumar, R. C. Rai, N. J. Podraza, S. Denev, M. Ramirez, Y.-H. Chu, L. W. Martin, J. Ihlefeld, T. Heeg, J. Schubert, D. G. Schlom, J. Orenstein, R. Ramesh, R. W. Collins, J. L. Musfeldt, and V. Gopalan, *Linear and nonlinear optical properties of $BiFeO_3$*, Appl. Phys. Lett. **92**, 121915 (2008).

[122] A. J. Hauser, J. Zhang, L. Mier, R. A. Ricciardo, P. M. Woodward, T. L. Gustafson, L. J. Brillson, and F. Y. Yang, *Characterization of electronic structure and defect states of thin epitaxial $BiFeO_3$ films by UV-visible absorption and cathodoluminescence spectroscopies*, Appl. Phys. Lett. **92**, 222901 (2008).

[123] R. Palai, R. S. Katiyar, H. Schmid, P. Tissot, S. J. Clark, J. Robertson, S. A. T. Redfern, G. Catalan, and J. F. Scott, *β phase and $\gamma - \beta$ metal-insulator transition in multiferroic $BiFeO_3$*, Phys. Rev. B **77**, 014110 (2008).

[124] S. H. Wemple, *Polarization Fluctuations and the Optical-Absorption Edge in $BaTiO_3$*, Phys. Rev. B **2**, 2679 (1970).

[125] J. Hlinka, J. Pokorny, S. Karimi, and I. M. Reaney, *Angular dispersion of oblique phonon modes in $BiFeO_3$ from micro-Raman scattering*, Phys. Rev. B **83**, 020101 (2011).

[126] H. Fukumura, H. Harima, K. Kisoda, M. Tamada, Y. Noguchi, and M. Miyayama, *Raman scattering study of multiferroic $BiFeO_3$ single crystal*, J. Magn. Magn. Mater. **310**, e367 (2007).

[127] M. Cazayous, D. Malka, D. Lebeugle, and D. Colson, *Electric field effect on $BiFeO_3$ single crystal investigated by Raman spectroscopy*, Appl. Phys. Lett. **91**, 071910 (2007).

[128] R. Palai, H. Schmid, J. F. Scott, and R. S. Katiyar, *Raman spectroscopy of single-domain multiferroic $BiFeO_3$*, Phys. Rev. B **81**, 064110 (2010).

[129] M. Cazayous, A. Sacuto, D. Lebeugle, and D. Colson, *Possible interplay between a two phonon mode and high energy magnetic excitations in $BiFeO_3$*, The European Physical Journal B **67**, 209 (2009).

[130] W. Hayes and R. Loudon, *Scattering of light by crystals*, John Wiley & Sons, Ltd., 1978.

[131] P. Yu and M. Cardona, *Fundamentals of semiconductors*, Springer, 2005.

[132] Y. Fujioka, J. Frantti, and M. Kakihana, *Franck-Condon Modes in Sr_2MnWO_6 Double Perovskite*, J. Phys. Chem. B **108**, 17012 (2004).

[133] J. Andreasson, J. Holmlund, R. Rauer, M. Käll, L. Börjesson, C. S. Knee, A. K. Eriksson, S.-G. Eriksson, M. Rübhausen, and R. P. Chaudhury, *Electron-phonon interactions in perovskites containing Fe and Cr studied by Raman scattering using oxygen-isotope and cation substitution*, Phys. Rev. B **78**, 235103 (2008).

[134] V. Shelke, D. Mazumdar, S. Jesse, S. Kalinin, A. Baddorf, and A. Gupta, *Ferroelectric domain scaling and switching in ultrathin $BiFeO_3$ films deposited on vicinal substrates*, ArXiv , 1010.0604 (2012).